AGU PUBLICATIONS

Tectonics

RESEARCH ARTICLE
10.1002/2015TC003835

Key Points:
- South China experienced orogenic events at 435–415 and 230–210 Ma
- Geochemical data on granitoids indicate only minor or no juvenile addition to the crust
- Geodynamic model for the two tectonothermal events suggests an intracratonic setting

Supporting Information:
- Tables S1–S4 captions
- Table S1
- Table S2
- Table S3
- Table S4

Correspondence to:
L. Shu,
lsshu@nju.edu.cn

Citation:
Shu, L., B. Wang, P. A. Cawood, M. Santosh, and Z. Xu (2015), Early Paleozoic and Early Mesozoic intraplate tectonic and magmatic events in the Cathaysia Block, South China, *Tectonics*, *34*, 1600–1621, doi:10.1002/2015TC003835.

Received 30 JAN 2015
Accepted 21 JUN 2015
Accepted article online 25 JUN 2015
Published online 8 AUG 2015

Early Paleozoic and Early Mesozoic intraplate tectonic and magmatic events in the Cathaysia Block, South China

Liangshu Shu[1,2], Bo Wang[1], Peter A. Cawood[3,4], M. Santosh[5], and Zhiqin Xu[6]

[1]State Key Laboratory for Mineral Deposits Research, Nanjing University, Nanjing, China, [2]Collaborative Innovation Center of Continental Tectonics, Xi'an, China, [3]Department of Earth Sciences, University of St. Andrews, St. Andrews, UK, [4]Centre for Exploration Targeting, School of Earth and Environment, University of Western Australia, Crawley, Western Australia, Australia, [5]School of Earth Sciences and Resources, China University of Geosciences Beijing, Beijing, China, [6]State Key Laboratory of Continental Tectonics and Dynamics, Institute of Geology, Chinese Academy of Geological Sciences, Beijing, China

Abstract The geodynamic framework of the South China Craton in the Early Paleozoic and Early Mesozoic has been modeled as developing through either oceanic convergence or intracontinental settings. On the basis of an integrated structural, geochemical, zircon U-Pb and Hf isotopic, and mica $^{40}Ar/^{39}Ar$ geochronologic study we establish that an intracontinental setting is currently the best fit for the available data. Our results suggest that widespread tectonomagmatic activity involving granite emplacement and mylonitic deformation occurred during two distinct stages: ~435–415 Ma and ~230–210 Ma. The coeval nature of emplacement of the plutons and their ductile deformation is corroborated by the subparallel orientation of the mylonitic foliation along the pluton margins, gneissose foliation in the middle part of pluton, the magmatic foliation within the plutons, and the schistosity in the surrounding metamorphosed country rocks. The 435–415 Ma granitoids exhibit peraluminous, high-K characteristics, and zircons show negative $\varepsilon Hf(t)$ values (average −6.2, $n = 66$), and Paleoproterozoic two-stage model ages of circa 2.21–1.64 Ga (average 1.84 Ga). The data suggest that the Early Paleozoic plutons were derived from the partial melting of the Paleoproterozoic basement of the Cathaysia Block. The 230–210 Ma granites are potassic and have zircons with $\varepsilon Hf(t)$ values of −2.8–−8.7 (average −5.4, $n = 62$), corresponding to T_{DM2} ages ranging from 2.0 to 1.44 Ga (average 1.64 Ga), suggesting that the Early Mesozoic partial melts in Cathaysia were also derived from basement. The geochemical distinction between the two phases of granites traces continental crustal evolution with time, with the Early Mesozoic crust enriched in potassium, silicon, and aluminum, but deficient in calcium, relative to the Paleozoic crust. Kinematical investigations provide evidence for an early-stage ductile deformation with a doubly vergent thrusting pattern dated at 433 ± 1 to 428 ± 1 Ma ($^{40}Ar/^{39}Ar$ furnace step-heating pseudoplateau ages obtained on muscovite and biotite from mylonite and deformed granite) and a late-stage strike-slip movement with sinistral sense of ductile shearing at 232 ± 1 to 234 ± 1 Ma ($^{40}Ar/^{39}Ar$ furnace step-heating pseudoplateau ages) along an E-W direction. The geological, geochemical, and isotopic signatures likely reflect far-field effects in response to continental assembly events at these times.

1. Introduction

The Proterozoic formation of the South China Craton, composed of the Yangtze and Cathaysia Blocks (Figure 1), and its subsequent Phanerozoic history of tectonomagmatic events, is an important component of the tectonic evolution of Asia [*W. X. Li et al.*, 2008; *Z. X. Li et al.*, 2008, 2009; *Rong et al.*, 2010; *Zhao and Cawood*, 2012; *Cawood et al.*, 2013; *Zhang and Zheng*, 2013; *Zhang et al.*, 2013]. Assembly of the craton occurred in the Neoproterozoic along a series of accretionary orogens that formed along the boundary between the constituent Yangtze and Cathaysia Blocks. The late Neoproterozoic to Phanerozoic records of crustal evolution of the craton involved periods of sediment accumulation interspersed with pulses of deformation and magmatism; the latter focused in the Cathaysia Block. The tectonic setting of the craton during this time period and in particular whether orogenic activity was situated at sites of oceanic subduction or in an intracontinental setting, removed from any plate margin, have been much debated [*Guo et al.*, 1989; *Chen et al.*, 1995, 2010; *Wang et al.*, 2010, 2013a; *Zhao and Cawood*, 2012; *Cawood et al.*, 2013; *Charvet*, 2013; *Zhang et al.*, 2013; *Shu et al.*, 2014].

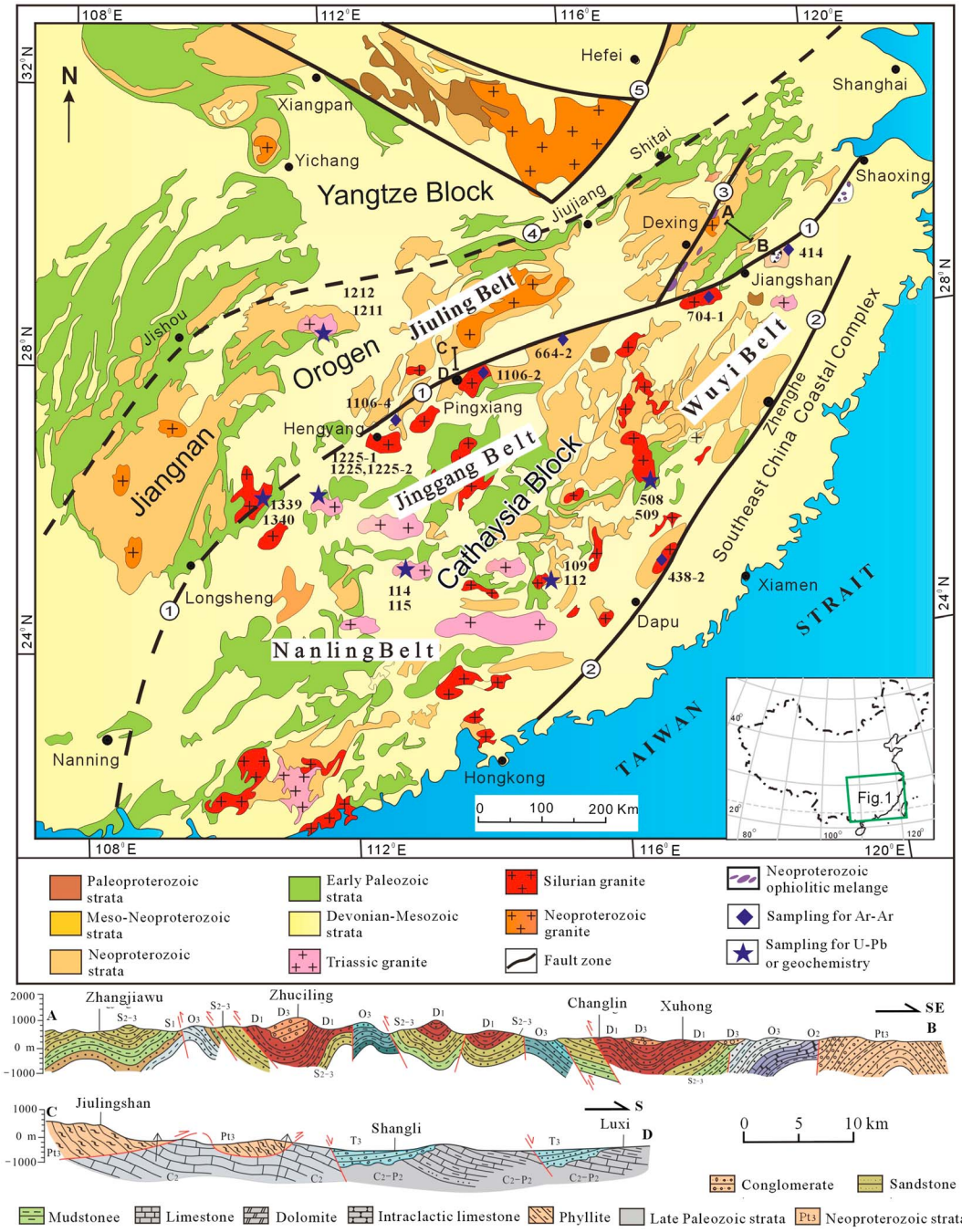

Figure 1. Geological sketch map of the South China Craton with cross sections A-B and C-D showing Early Paleozoic and Early Mesozoic deformation. 1: Shaoxing-Pingxiang boundary fault zone between Yangtze and Cathaysia Blocks; 2: Zhenghe-Dapu boundary fault zone between the Cathaysia basement and the SE-China Coastal Complex; 3: Northeast Jiangxi Neoproterozoic ophiolitic zone; 4: Jiujiang-Shitai buried fault zone of the northern boundary of the Jiangnan Belt; and 5: Tanlu sinistral strike-slip fault zone.

The identification of ophiolitic rocks of inferred Early Paleozoic age in the Cathaysia Block [*Guo et al.*, 1989; *Wang and Mo*, 1995] was interpreted as evidence for subduction and accretion of an oceanic plate forming the Wuyi and Yunkai orogenic belts [*Guo et al.*, 1989] that was subsequently reworked in a well-developed fold-thrust system during the Early Mesozoic [*Xiao and He*, 2005]. Kyanite-bearing pelitic schists/gneisses were identified in the northern Cathaysia Block, which experienced pressures of up to 10 kbar [*Zhao and Cawood*, 2012]. Hence, the Cathaysia Block was considered to represent a

continent-continent collisional belt along which the South China Craton collided with an unknown continental block that was later removed by rifting [*Zhao and Cawood*, 2012].

Integrated investigations in the past decade suggest that previous convergent plate models do not adequately explain the tectonic setting of Cathaysia. These new data include the fact that almost all basaltic layers in the Early Paleozoic strata have been redefined as metagraywacke [*Shu*, 2006; *Shu et al*., 2008a, 2014; *Xiang and Shu*, 2010; *Yao et al*., 2011], and gabbro samples from ophiolitic rocks previously considered as Early Paleozoic yielded zircon U-Pb ages of 850–800 Ma [*Li et al*., 2005, 2010; *Shu et al*., 2006, 2011]. Stratigraphically, a two-stage stable depositional environment can be recognized in the Paleozoic: a sandy-muddy sequence that accumulated in the Cambrian to Late Ordovician [*Chen et al*., 1995, 2010, 2012; *Wang et al*., 2010; *Zhang et al*., 2013; *Shu et al*., 2014], and a carbonate sequence that formed in the Carboniferous to Early Triassic [*Shu et al*., 2008b; *Shu*, 2012]. Silurian and Middle Triassic strata are absent in the Cathaysia Block. Ophiolite, volcanic rock or high pressure/low temperature (LT) metamorphic rock has not been found in the Paleozoic strata of the Cathaysia Block. Hence, the subduction or collision models of plate margin interaction [*Guo et al*., 1989; *Hsü et al*., 1990] are not supported by currently available data.

Granitoids and ductile deformed Proterozoic to Early Paleozoic country rocks are widespread in the Cathaysia Block and include more than 200 pre-Jurassic plutons exposed over an area of 25,000 km^2 [*Zhou et al*., 2006; *Shu et al*., 2008a; *Wang and Shu*, 2012]. However, the petrogenesis of granitic plutons and the ages of ductile deformation are still unclear with only rare isotopic age data available for constraining the timing of deformation. Whether the granitic magmas were generated prior to, or coeval with deformation, remains equivocal.

In this paper, we present geologic, structural, geochemical, and laser ablation inductively coupled plasma–mass spectrometry (LA-ICP-MS) zircon U-Pb and Hf isotopic data of granitic plutons and $^{40}Ar/^{39}Ar$ analyses on muscovite and biotite from deformed granites and mylonitic country rock. Our results document two episodes of tectonomagmatic activity and provide constraints on the magma sources associated with the evolution of the Cathaysia Block during the Paleozoic and Mesozoic.

2. Geological Setting

A series of convergent plate margin accretionary rocks dated between 930 and 800 Ma constitute the Jiangnan Orogen and delineate the assembly of the Yangtze and Cathaysia Blocks into the South China Craton. The northeast striking Shaoxing-Pingxiang fault zone, marks the northwestern boundary of the Cathaysia Block and its eastern boundary extends beyond the eastern shoreline of mainland China (Figure 1). Three belts (Wuyi, Jinggang, and Nanling) (Figure 1) are exposed in eastern Cathaysia. The Wuyi Belt is characterized by high-grade metamorphic assemblages of Paleozoic and Neoproterozoic rock units [*Yu et al*., 2009; *Xu et al*., 2014] with almost no Early Paleozoic units, whereas the Jinggang and Nanling belts contain only Neoproterozoic and Early Paleozoic strata. Two pre-Devonian lithotectonic units comprising the low-grade metamorphic rocks and basement, respectively, have been recognized in these belts [*Faure et al*., 2009; *Shu et al*., 2014].

The low-grade metamorphic unit is composed of a late Neoproterozoic (Sinian) to Ordovician sandstone-mudstone slate sequence [*Shu*, 2006; *Shu et al*., 2008a; *Wang et al*., 2010; *Zhang et al*., 2013]. The basement unit is represented by early Neoproterozoic sandstone, mudstone, and volcanic rocks (basalt, basaltic andesite, rhyolite, and volcanoclastic rock) in the Jinggang-Nanling area and Paleoproterozoic granites, sedimentary, and basaltic rocks in the Wuyi domain [*Li*, 1997; *Yu et al*., 2009], which were later metamorphosed into schist, amphibolite, gneiss, and orthogneiss [*Zhao and Cawood*, 1999].

Early Paleozoic sedimentary facies extend across South China with the Cambrian to Ordovician succession ranging from carbonate sequences in the Yangtze Block to carbonate-siliceous sequences in the region of the Jiangnan orogen and *graptolite*-bearing sandy-muddy sequences in the Cathaysia Block displaying a $>$1000 km wide stable depositional environment ranging from platform margin to slope [*Chen et al*., 1995, 2012; *Shu et al*., 2008a, 2014; *Wang et al*., 2010; *Rong et al*., 2012]. A regional-scale tectonomagmatic event took place in the Cathaysia during the Early Paleozoic [*Ren and Chen*, 1989; *Ren et al*., 1990; *Ren*, 1991; *Li et al*., 2010; *Xu et al*., 2011; *Zhang et al*., 2011, 2013]. This event triggered folding, thrusting (cross-section

A-B, Figure 1) and large-scale crustal anatexis with the emplacement of granites and lower greenschist facies metamorphism constituting the South China Fold Belt.

Since the Middle or Late Devonian, the entire South China region evolved into a more stable littoral-neritic depositional environment [*Zhang et al*., 2013], characterized by *Brachiopoda*-, *coral*-, and *Fusulina-bearing* carbonate depositional platform containing limestone, dolomite, black chert, and minor sandstone and mudstone [*Shu et al*., 2008b]. In the Triassic, further tectonomagmatic activity affected the region with almost all pre-Triassic rocks incorporated into a regional fold-thrust system (cross-section C-D, Figure 1). Peraluminous granites were emplaced, mainly in the Nanling belt (Figure 1) at 240–200 Ma [*Zhou et al*., 2006; *Wang et al*., 2007b, 2014]. Pre-Mesozoic deformation structures are unconformably overlain by the Late Triassic coarse-grained clastic rocks (cross-section C-D, Figure 1), suggesting that the South China region was intensely reworked by Early Mesozoic tectonism and magmatism. Further igneous activity occurred in the Late Mesozoic and is dated at 140–100 Ma, extending over the 200–400 km wide southeast China coastal complex zone (Figure 1) [*Wang and Zhou*, 2002; *Zhou et al*., 2006; *Li et al*., 2012; *Wang and Shu*, 2012]. This magmatic event is attributed to NW directed subduction of the Pacific plate beneath East Asia in the Late Mesozoic.

3. Field Occurrence and Sample Description

3.1. Samples With Ductile Deformation Structures

Three phases of ductile deformation have been identified in pre-Mesozoic rocks of the Cathaysia Block. The first phase (D1), recognized in the Wuyi and Jiuling belts, is marked by recumbent folds with sub-E-W trending axial planes in the Neoproterozoic strata. Contemporaneous southeast directed thrusting is developed in the Jiangnan Orogen [*Charvet et al*., 2010].

The second phase (D2) is developed throughout pre-Devonian strata in Cathaysia and is characterized by macroscopic flexural slip folds with tight to isoclinal profiles and sub-E-W trending axes (cross-section A-B, Figure 1). Folding was accompanied by regional-scale ductile thrusting that yielded mylonitic rocks with shear foliation and a stretching lineation plunging 40–50° to the southeast in the NW Cathaysia and plunging 50–60° to the northwest in the SE Cathaysia. D2 is the dominant deformation event in Cathaysia.

The third phase (D3) is characterized by a late reworking displayed in gentle folds with a NE trending axial plane that partially overprinted preexisting D2 structures. Near or along the northwestern boundary of the Cathaysia Block, well-developed strike-slip structures with subvertical foliation and subhorizontal stretching lineation cut ductile thrusting structures of the first two phases of deformation. On the southern slope of the Jiuling Mountains, D3 deformation is characterized by symmetric upright folds with subvertical axial planes and subhorizontal hinge lines that are associated with south verging faulting (cross-section C-D, Figure 1).

To constrain the timing of deformation, six mica samples were collected for $^{40}Ar/^{39}Ar$ dating from muscovite schist, two-mica granite, deformed K-granite, and orthogneiss in different locations (Figure 1). Petrologic features of the samples are given in Figure 2 and Table 1.

3.2. Granitoids

Three types of granitoids can be distinguished on the basis of modal abundance of the rock-forming minerals: K-feldspar granite, muscovite-biotite granite, and monzonite granite. The K-feldspar granite (Figures 2a and 2b) is characterized by high alkali-feldspar content (55–60% microcline, orthoclase, and perthite). These plutons often occur within a domal structure with development of mylonitic foliation and stretching lineation around its margin. The muscovite-biotite granite (Figures 2c and 2d) is mica enriched (~5–10% muscovite and 10–15% biotite), and the monzonitic granite (Figures 2e and 2f) consists of albitic plagioclase (15–25%), alkali-feldspar (30–35%), quartz (25–35%), biotite (10–15%), and muscovite (1–3%). Most granites show chilled margins composed of microcline and quartz grains.

Two phases of granitoid magmatism can be established from field relations. In the first, granites cut metamorphosed Neoproterozoic to Ordovician rocks and are unconformably overlain by the Middle to Upper Devonian coarse-grained clastic rocks [*Shu et al*., 2014]. During the second phase, granitic bodies intruded the Late Paleozoic sedimentary rocks and the older granites.

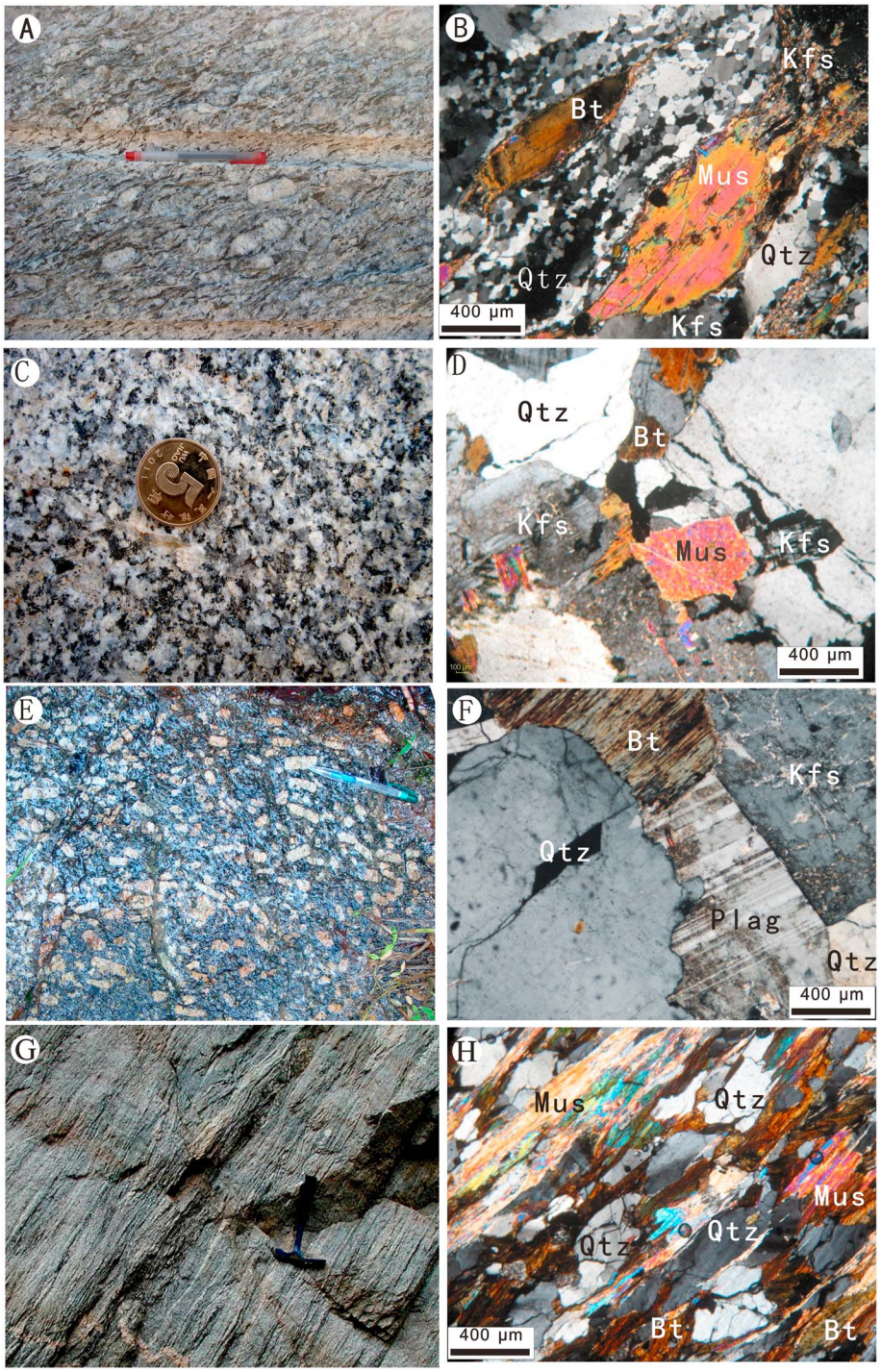

Figure 2. Field photos and photomicrographs of samples analyzed in this study. (a) Field photograph of sample 112 (deformed K-granite) in Fuxi of the Nanling belt. (b) Photomicrograph of sample 112 (crossed nicols). (c) Field photograph of sample 1212 (muscovite-biotite-granite) in Shatianwan of Taojiang of the Jiangnan belt. (d) Photomicrograph of sample 1212 (crossed nicols). (e) Field photograph of sample 1225-1 (monzonitic granite) in Tangjiawan of the Cathaysia Block. (f) Photomicrograph of sample 1225-1 (crossed nicols). (g) Filed photograph of sample 414 (mica schist) in the northern Zhenghe of the Cathaysia Block. (h) Photomicrograph of sample 414 (crossed nicols). Kfs, K-feldspar; Plag, plagioclase; Qtz, quartz; Mus, muscovite; Bt, biotite.

Table 1. Petrographic Features of Samples With GPS Locations

Sample Number	GPS Location	Texture	Structure	Mineralogy	Rock Name
1339, 1340	N26°02.765′, E110°35.408′	Porphyroidal	Oriented, foliated	Phenocryst 25%: microcline 15%, quartz 8–10%, and biotite 2–3%; fine-grained groundmass 75%: microcline 25%, albite 3–5%, quartz 25%, biotite 15–20%, and muscovite 5–10%; accessory minerals (2–3%): pyrite, tourmaline, and zircon	K-feldspar granite
112, 109	N25°08.00′, E115°05.650′	Porphyroidal	Augen, gneissoid	Augen phenocryst 35%: microcline 20–25%, quartz 10–15%; fine-middle-grained groundmass 65%: microcline 30%, albite 2–3%, quartz 15–20%, and biotite 15%; accessory minerals (2–3%): pyrite, tourmaline, monazite, and zircon	K-feldspar granite
508, 509	N26°20.23′, E116°10.770′	Porphyroidal	Augen, gneissoid	Augen phenocryst 30%: microcline 15–20% and quartz 10–15%; middle-grained groundmass 70%: microcline 25%, quartz 20–25%, biotite 15–20%, and muscovite 5%; accessory minerals (2–3%): pyrite, apatite, and zircon	K-feldspar granite
1212, 1211	N28°29.725′, E112°04.265′	Porphyroidal	Weak oriented, massive	Phenocryst 20%: microcline 15% and quartz 5%; fine-middle-grained groundmass 80%: microcline 35%, albite 3–5%, quartz 25–30%, biotite 10–15%, and muscovite 5–10%; accessory minerals (1–2%): pyrite and zircon	Muscovite-biotite-granite
114, 115	N25°11.093′, E112°50.965′	Middle grained	Massive	Microcline 35–40%: quartz 30–35%, muscovite 10–12%, albite 15%, biotite 5–10%; accessory minerals (rare)	Muscovite granite
1225-1, 1225, 1225-2	N26°08.793′, E111°44.685′	Middle grained, porphyroidal	Oriented, foliated	Phenocryst 20–25%: microcline 15% and quartz 5–10%; middle-grained groundmass 75%: microcline 20%, albite 15–25%, quartz 20%, biotite 10–15%, and muscovite 2–3%; accessory minerals (2–3%): pyrite, tourmaline, apatite, and zircon	Monozitic granite
664-2	N28°18.983, E115°09.141′	Metacrystic	Foliation, stretching lineation	Quartz 55%, potash feldspar + albite 25–30%, muscovite 5%, bioite 2–5%, and sericite + chlorite 10%	Quartz-feldspar mylonite
704-1	N29°00.434′, E117°02.083′	Porphyroidal	Oriented, foliated	Oriented phenocrysts (35%): potash feldspar + sanidine 10%, quartz 20%, albite 3%, and biotite 2–3%; Fine-grained groundmass (60–65%): quartz + albite 50%, mica 3–5%, and scaly-like sericite + chlorite 10%; accessory minerals (1–3%): zircon and titanite	Monzonitic granite
438-2	N25°17.230′, E116°18.223′	Fine-middle grained	Massive	Microcline 35%, sanidine 10%, quartz 30%, biotite 10–15%, and muscovite 10–12%; accessory minerals (2–4%): zircon, titanite, and aptite	Muscovite-biotite-granite
1106-2	N28°01.483′, E113°54.364′	Fine-middle grained	Oriented, foliated	Oriented phenocryst 25%: microcline 15%, quartz 5–10%, and biotite 3–5%; groundmass 75–80%: microcline 30%, albite 3–5%, quartz 25%, biotite 10–12%, and muscovite 3–5%; accessory minerals (1–3): pyrite and hematite	K-feldspar granite
414	N29°41.423, E118°18.321′	Metacrystic	Foliation, lineation	Quartz 50%, potash feldspar 10–15%, muscovite 15–20%, albite 10–15%, bioite 5%, and sericite + chlorite 10%	Muscovite schist
1106-4	N27°36.831′, E112°48.533′	Metacrystic	Foliation, stretching lineation	Quartz 45–50%, potash feldspar 15–20%, biotite 15–20%, albite 15%, muscovite 5–10%, and sericite + chlorite 5–10%	Biotite schist

AGU Tectonics

10.1002/2015TC003835

Several dome-forming granitic plutons display distinct zoning with massive granite in the core, gneissose granite (orthogneiss) in the middle, and mylonitic rocks around the margin, indicating a deformed process of falling temperatures. The granites in different zones have similar crystallization ages and geochemical compositions [*Zhang et al*., 2011], suggesting coeval magmatism from the same source. The gneissosity in the midway region between the core and rim is defined by mylonitic foliation with a weak stretching lineation. This fabric and the magmatic foliation within the pluton are parallel and similar to the trends of the mylonitic foliation with a well-developed lineation on the margin of pluton and with the schistosity in the surrounding metamorphic rocks [*Charvet et al*., 2010; *Zhang et al*., 2011; *Shu et al*., 2014]. These features suggest magmatism was synchronous with Early Paleozoic and Early Mesozoic metamorphism and deformation in Cathaysia.

Six samples, three from the Early Paleozoic and three from the Early Mesozoic intrusions were collected for zircon U-Pb dating and in situ Lu-Hf isotope analysis. Thirteen granitic samples (six from the Early Paleozoic and seven from Early Mesozoic granites, including the six collected for isotopic analysis) were analyzed for major, rare earth element (REE) and trace elements. The sampling localities are shown in Figure 1. GPS locations and petrological features of the samples are listed in Table 1.

4. Analytical Procedures and Results

4.1. Geochemical Analysis

The major element compositions were determined using a VF-320 X-ray fluorescence spectrometer at the Center of Modern Analysis (Nanjing University). FeO contents were analyzed by wet chemistry. Analytical uncertainties were estimated to be better than 5% for major elements following the analytical procedure described by *Franzini et al*. [1972]. The concentrations of rare earth and other trace elements were analyzed using a Finnigan MAT Element II-type ICP-MS at the State Key Laboratory for Mineral Deposits Research (Nanjing University). The working conditions and analytical procedures are described by *Qi and Gregoire* [2000a, 2000b]. The analytical precision for most elements is better than 5%. The chondrite values [*Sun and McDonough*, 1989] are used as the representation of the REE patterns, whereas the primitive mantle values [*McDonough and Sun*, 1995] are used to construct the multielement spidergrams. The analytical results of major, REE and trace elements are listed in Table S1 in the supporting information.

4.2. LA-ICP-MS Zircon U-Pb Dating

Zircon grains for U-Pb dating were separated using conventional techniques of heavy liquid and magnetic separation, followed by handpicking under a binocular microscope. The zircon grains were mounted in epoxy resin and polished. Cathodoluminescence (CL) images of the zircons were obtained using an electron microscope (Quanta 400 FEG) with a Mono CL3+ (Gatan, USA) at the State Key Laboratory of Continental Dynamics in the Northwest University, Xi'an.

Zircon U-Pb isotopic analyses were performed using an Agilent 7500a ICP-MS attached to a New Wave 213 nm laser ablation system with an in-house sample cell, at the State Key Laboratory for Mineral Deposits Research, Nanjing University. During the analyses, a laser beam spot size of ~30 μm in diameter and a laser frequency of 5 Hz and 60% energy were used. The U-Pb fractionation has been corrected by zircon standard GEMOC GJ-1 ($^{207}Pb/^{206}Pb$ age of 608.5 ± 1.5 Ma) [*Jackson et al*., 2004], and accuracy was controlled using the Mud Tank zircon standard (an intercept value of 732 ± 5 Ma) [*Black et al*., 2003]. The analytical procedure in this study is similar to those described in *Griffin et al*. [2004], *Wang et al*. [2010], and *Ma et al*. [2012]. U-Th-Pb age calculations and concordia diagrams were made using the ISOPLOT/Ex program (version 2.49) [*Ludwig*, 2001]. Weighted mean $^{206}Pb/^{238}U$ ages are quoted at 1σ error with 95% confidence level. The results of zircon U-Pb dating are listed in Table S2.

4.3. In Situ Lu-Hf Isotope of Zircons

In situ Lu-Hf isotope analyses were performed at Ministry of Land and Resources (MLR) Key Laboratory of Metallogeny and Mineral Assessment, Institute of Mineral Resources, Chinese Academy of Geological Sciences, Beijing, using a New Wave UP213 laser ablation microprobe, attached to a Neptune multicollector ICP-MS. Instrumental conditions and data acquisition are similar to those described in detail by *Wu et al*. [2006] and *Hou et al*. [2007]. A stationary spot with a beam diameter of 35 μm was used during analysis.

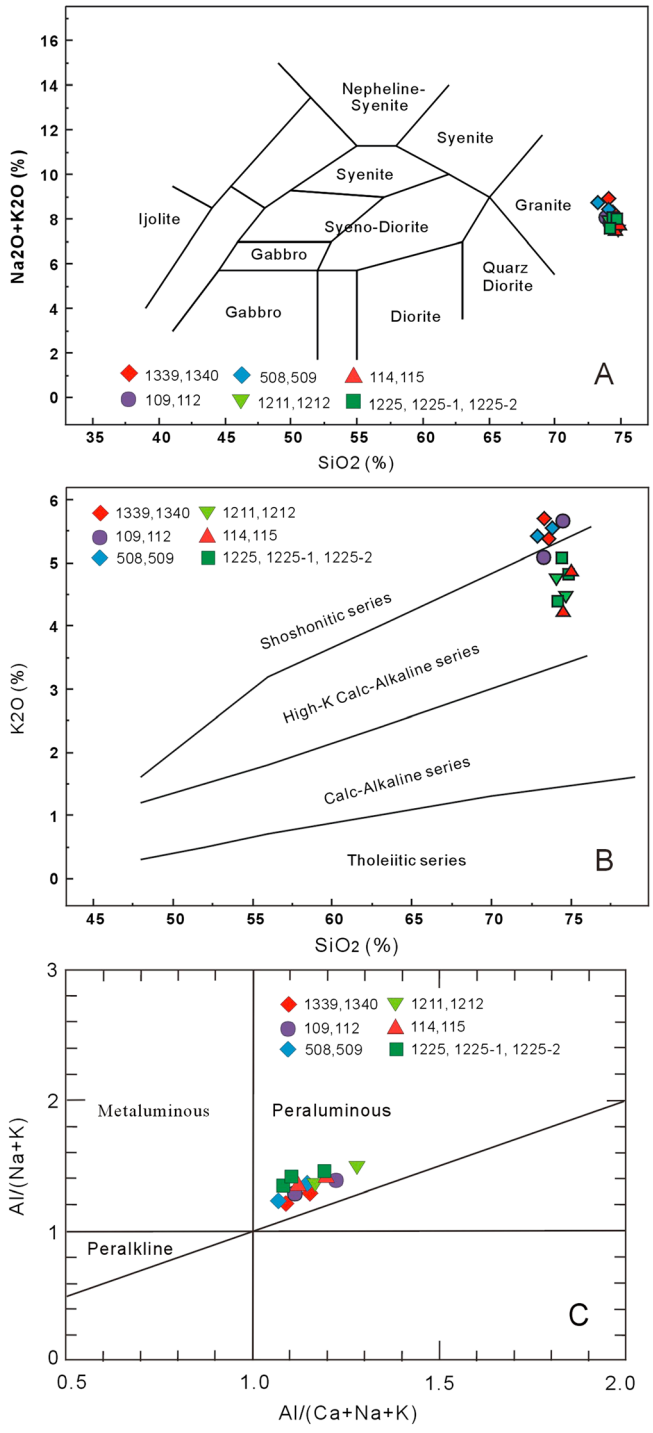

Figure 3. Geochemical features of the granitoids in the study area. (a) ($K_2O + Na_2O$) versus SiO_2 diagram [*Cox et al.*, 1979]; (b) K_2O versus SiO_2 diagram [*Rickwood*, 1989], and (c) Shand's index Al/(Na + K) vesrus Al/(Ca + Na + K) plots [*Maniar and Piccolli*, 1989].

Helium was used as the carrier gas to transport the ablated sample from the laser ablation cell to the ICP-MS torch via a mixing chamber mixed with argon.

In order to correct the isobaric interferences of ^{176}Lu and ^{176}Yb on ^{176}Hf, the ratios $^{176}Lu/^{175}Lu = 0.02658$ and $^{176}Yb/^{173}Yb = 0.796218$ were determined [*Chu et al.*, 2002]. For instrumental mass bias correction Yb isotope ratios were normalized to $^{172}Yb/^{173}Yb$ of 1.35274 [*Chu et al.*, 2002] and Hf isotope ratios to $^{179}Hf/^{177}Hf$ of 0.7325 using an exponential law. The mass bias behavior of Lu was assumed to follow that of Yb with mass bias correction protocols described by *Wu et al.* [2006] and *Hou et al.* [2007]. Zircon GJ1 was adopted as reference standard during our routine analyses, with a weighted mean $^{176}Hf/^{177}Hf$ ratio of 0.282007 $\pm$ 0.000007 (2σ, $n = 36$). This value is indistinguishable from the weighted mean $^{176}Hf/^{177}Hf$ ratio of 0.282000 $\pm$ 0.000005 (2σ) determined by solution analysis [*Morel et al.*, 2008]. A decay constant for ^{176}Lu of 1.867×10^{-11} year^{-1} [*Soderlund et al.*, 2004] was calculated for initial $^{176}Lu/^{177}Hf$ ratios. The εHf(t) value was used as calculation by assuming chondritic values of $^{176}Lu/^{177}Hf = 0.282785$ and $^{176}Hf/^{177}Hf = 0.0336$ [*Bouvier et al.*, 2008]. The two-stage model age (T_{DM2}) was calculated for the source rock of magma using $^{176}Lu/^{177}Hf = 0.015$ for the average continental crust [*Griffin et al.*, 2002], the T_{DM2} relative to average continental crust was chosen only when the εHf(t) values are notably negative. The analyzed Lu-Hf isotopic compositions are listed in Table S3.

4.4. Mica ^{40}Ar/^{39}Ar Dating

Separates for $^{40}Ar/^{39}Ar$ dating of muscovite and biotite from deformed granite and mylonite were prepared by handpicking the sieve fraction under a binocular zoom microscope and subsequent ultrasonic cleaning in demineralized water. Pure and fresh mineral fractions were wrapped in Al foil cylinders and then together with neutron flux monitors (LP-6 biotite) were irradiated in VT-C position at the Tsing-Hua Open-Pool Reactor for 30 h at Tsing-Hua University, Taiwan. $^{40}Ar/^{39}Ar$ analysis was conducted at the National Taiwan University. Step heating was

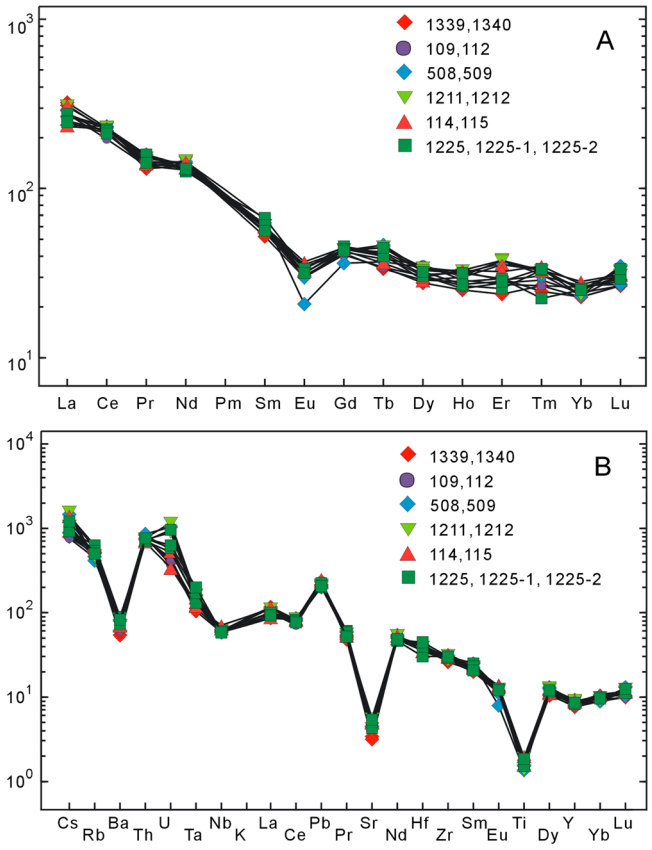

Figure 4. (a) Chondrite-normalized REE diagrams for the granitic rocks (the normalization values are from *Sun and McDonough* [1989]) and (b) primitive mantle-normalized trace element patterns for the granites (the normalization values are from *McDonough and Sun* [1995]).

carried out using a double vacuum Mo resistance furnace, the released gas was further purified through a Ti sponge furnace at 700°C and two Zr-Al getters, and argon isotopes were finally analyzed with a VG1200 mass spectrometer. *J* values were calculated from the gas composition released from the LP-6 biotite monitor with a calibrated $^{40}Ar/^{39}Ar$ age of 128.4 ± 0.2 Ma based on Fish Canyon Sanidine (28.201 ± 0.046 Ma) [*Kuiper et al*., 2008]. All isotopic measurements are corrected for mass discrimination and atmospheric argon contamination, following *Lee et al*. [2006] and *Mark et al*. [2011]. Decay constants used are after *Renne et al*. [2010, 2011]. The whole analyzing processes and age calculations were performed according to the procedures described by *Lo et al*. [2002]. $^{40}Ar/^{39}Ar$ results for the mica minerals are listed in Table S4.

5. Results

5.1. Geochemical Characteristics

The major element compositions of 13 granitic samples are similar with high SiO_2 (72.96–75.03%), Al_2O_3 (13.31–14.53%), and K_2O (4.23–5.72%). K_2O is higher than Na_2O (2.56–3.12%), and the A/CNK $(Al_2O_3/CaO + Na_2O + K_2O)_{MOL}$ values show a range of 1.1–1.3 (Table S1), establishing the strongly peraluminous *S*-type nature of the samples (see also Figure 3c). On the SiO_2 versus Na_2O+K_2O diagram [*Cox et al*., 1979], all samples fall in the granite field (Figure 3a), whereas on the SiO_2 versus K_2O diagram [*Rickwood*, 1989], six Early Paleozoic granitic samples plot in the shoshonitic series, whereas the seven Early Mesozoic granitic samples fall in the high-K calc-alkaline series (Figure 3b).

The rocks show high total rare earth elements (REEs; 335–374 ppm) (Table S1) with (La/Yb)*n* around 7.8–13.3 (mean of 13 analyses is 10.4) and exhibit light REE-enriched patterns (Figure 4), with a marked negative Eu anomaly (average Eu/Eu* of 0.6) for chrondite normalized values (Figure 4a and Table S1) [*Sun and McDonough*, 1989]. On primitive mantle-normalized spidergrams (Figure 4b) [*McDonough and Sun*, 1995] the samples show distinct Ba, Sr, Nb, and Ti negative anomalies, typical of granitic rocks derived from upper crustal source [*Pearce et al*., 1984; *Pearce*, 1996]. Nb/Ta values range from 5.3 to 10.6 (average 7.9), consistent with the geochemical features of crustal-derived granite [*Pearce et al*., 1984; *Pearce*, 1996]. Zr/Hf is around 25.2–36.9 (average 28.6); with the Early Paleozoic granites showing relatively lower values. All Th/U values are greater than 0.5 (average 1.3), consistent with the magmatic origin of zircons in these rocks.

On tectonic discrimination diagrams, the samples plot either in the postcollision (Figure 5a) or the late and postcollision (Figure 5b) fields.

5.2. Zircon U-Pb Dating

Zircons analyzed in this study range in length from 100 to 160 μm, and with length/width ratios of about 2:1. They show variable abundance of Th (86–1313 ppm) and U (168–714 ppm), and high Th/U ratios (from 0.51 to 1.84) (Table S2). Most of the zircons display oscillatory or linear zoning in the CL images (Figure 6), indicating

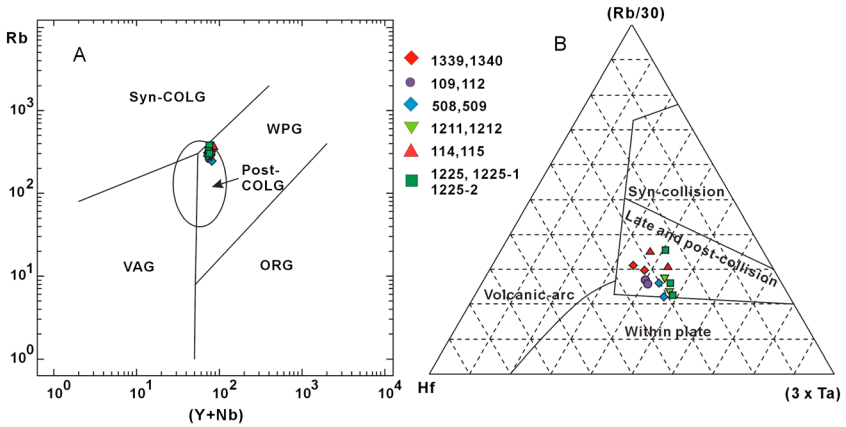

Figure 5. Tectonic discrimination diagrams for the granites. (a) (Y + Nb)-Rb plot [after *Pearce*, 1996]; (b) Rb/10-Hf-3Ta plot [after *Harris et al.*, 1986].

Figure 6. Representative Cathodoluminescence (CL) images for the granitic rocks from the study area. See Table S2 for individual analyses, corresponding isotopic ratios and ages.

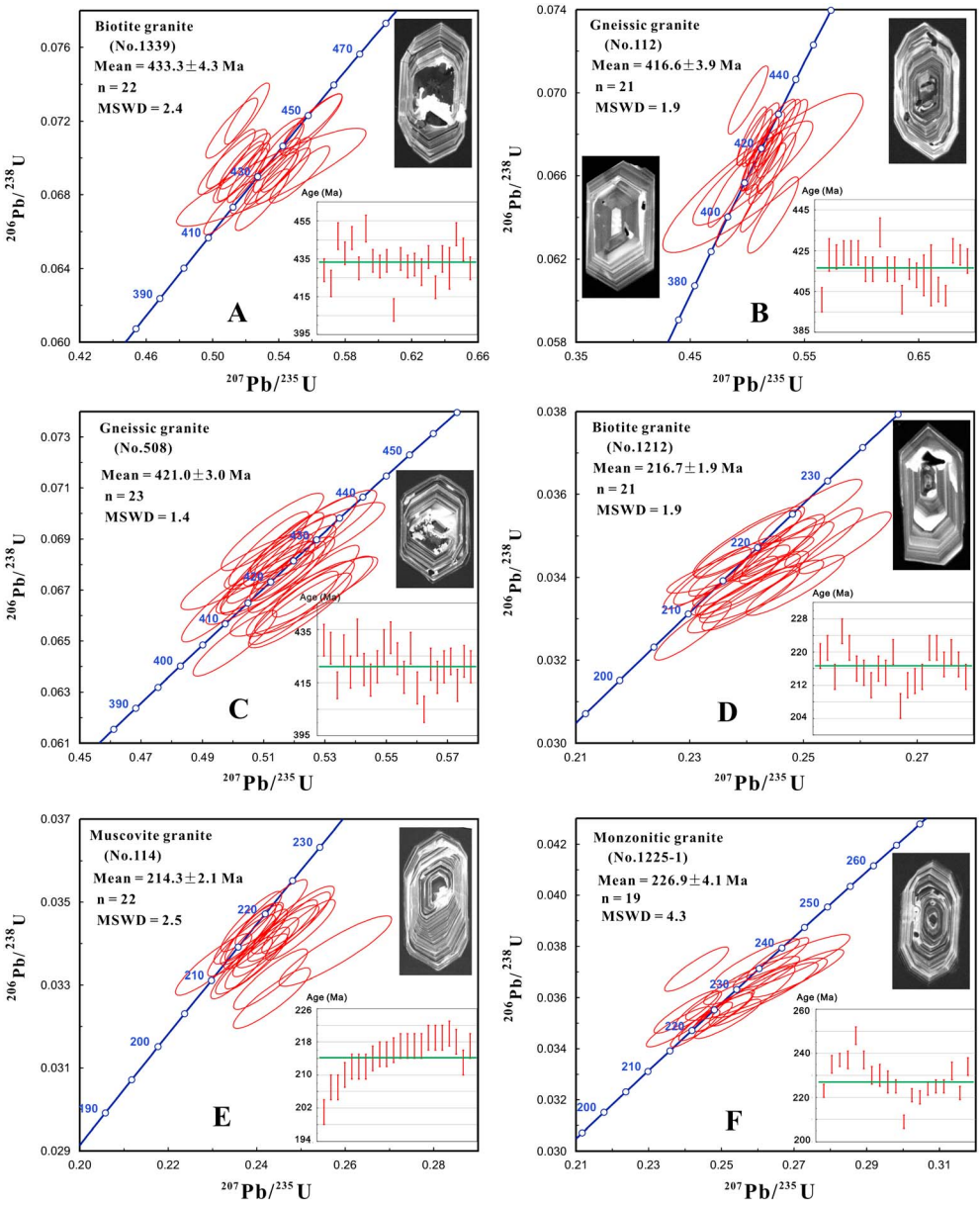

Figure 7. (a–f) Concordia $^{206}Pb/^{238}U$-$^{207}Pb/^{235}U$ diagrams from LA-ICP-MS U-Pb data for zircon grains from six granitic plutons.

that they preserve primary crystallization ages. Some zircon grains show distinct core-rim structures, in which the cores have a subrounded form with distinctly older ages, and are interpreted as inherited grains [*Hoskin and Black*, 2000] (Figure 6).

U-Pb analyses on euhedral zircons from samples of the Jinshan (sample 1339), Fuxi (112), and Jingfengsi (508) plutons define mean $^{206}Pb/^{238}U$ ages of 433.3 ± 4.3 Ma (n = 22, mean square weighted deviation (MSWD) = 2.4) (Figure 7a), 416.6 ± 3.9 Ma (n = 21, MSWD = 1.9) (Figure 7b), and 421.0 ± 3.0 Ma (n = 23, MSWD = 1.4) (Figure 7c), respectively. The ages are interpreted to represent the crystallization age of these rocks.

Zircons from the Shatianwan (sample 1212), Wenshao (114), and Tangjiawan (1225) plutons (Figure 1) yield $^{206}Pb/^{238}U$ ages of 216.7 ± 1.9 Ma (n = 21, MSWD = 1.9) (Figure 7d), 214.3 ± 2.1 Ma (n = 22, MSWD = 2.5) (Figure 7e), and 226.9 ± 4.1 Ma (n = 19, MSWD = 4.3) (Figure 7f), respectively. The dated grains show oscillatory zoning and a euhedral shape (Figures 7d–7f), and their age range of 230–215 Ma is interpreted as the best estimate of the crystallization age of these plutons.

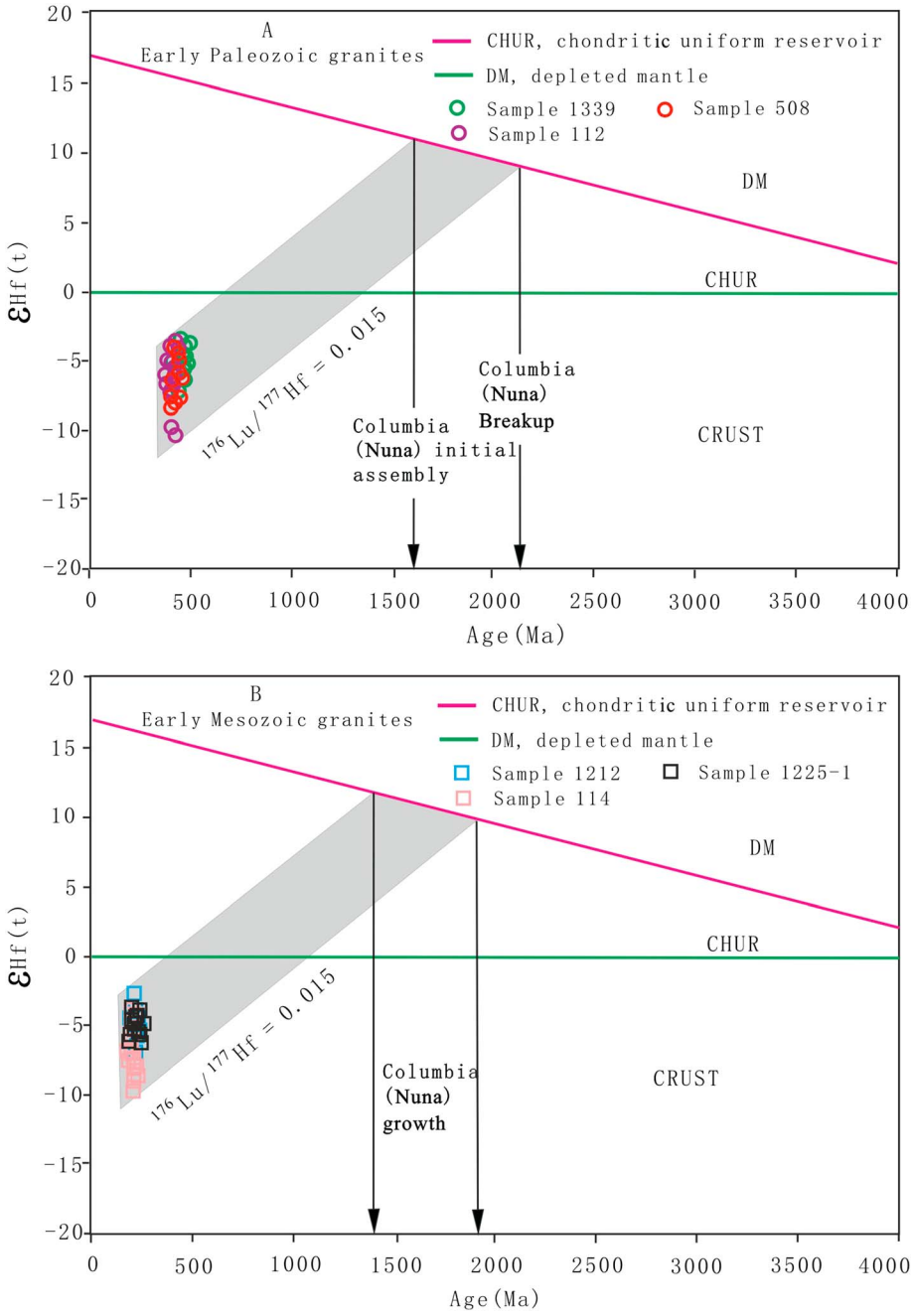

Figure 8. Epsilon Hf versus U-Pb age for the zircon grains from six granitic bodies ((a) Early Paleozoic granites; (b) Early Mesozoic plutons).

Some inherited zircon grains are present in the six samples analyzed, as evidenced from their significantly older ages. A total of 21 U-Pb ages, ranging from 1900 Ma to 550 Ma (Table S2), define five peaks that correspond to polyphase crustal evolution of the Cathaysia basement. These older age data suggest that the Cathaysia basement might be a principal source of the granites, although geological and magmatic records for the interval circa 600–550 Ma are currently sparse in Cathaysia.

5.3. In Situ Zircon Lu-Hf Isotopes

Lu-Hf isotopic data for the six granitic samples (three for Silurian and three for Triassic) are similar (Table S3). All samples show negative $\varepsilon Hf(t)$ values, with a mean of −4.9 to −6.8. Their average two-stage model ages

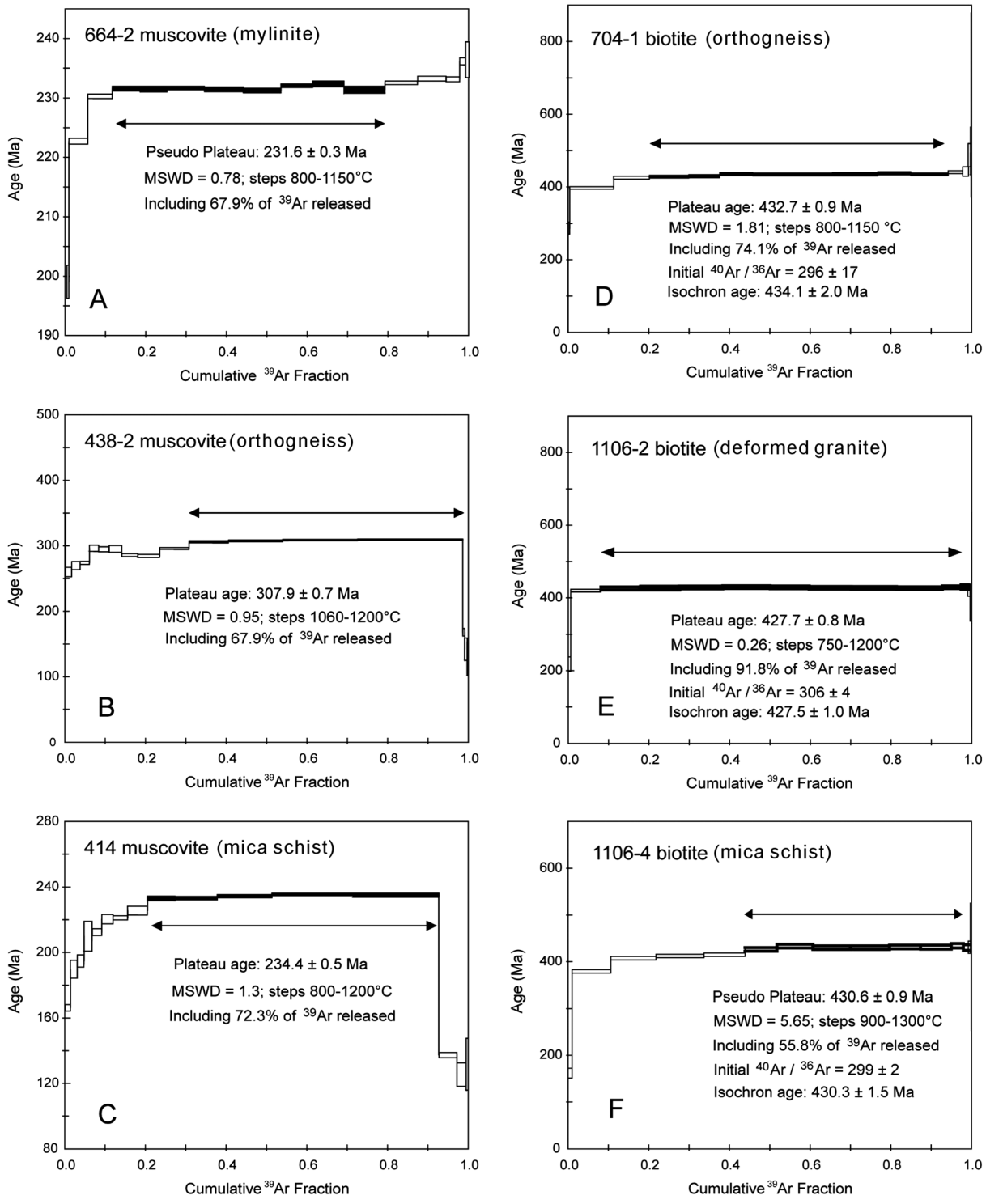

Figure 9. (a–f) Age spectra of $^{40}Ar/^{39}Ar$ dating results for biotite and muscovite from six samples collected from the southern and northern boundaries of the Cathaysia basement.

(T_{DM2}) are 1572–1924 Ma. On plots of $\varepsilon Hf(t)$ values versus crystallization ages (Figure 8) almost all analyzed zircons plot in a narrow domain with two-stage model ages of 1650–2200 Ma (T_{DM2}) and $\varepsilon Hf(t)$ values of −3.3 to −10.8 for the Silurian plutons (Figure 8a), and model ages of 1440–2000 Ma (T_{DM2}) and $\varepsilon Hf(t)$ values of −2.8 to −10.0 for the Triassic granites (Figure 8b). These features suggest that the zircons from

either the Silurian or Triassic granites were derived from the reworking of the Cathaysia crust with Paleozoic and Mesoproterozoic ages and that the involvement of a mantle component was insignificant.

5.4. Mica $^{40}Ar/^{39}Ar$ Dating Results

The $^{40}Ar/^{39}Ar$ analytical results are shown in Table S4 and plotted as age spectra in Figure 9. The errors are quoted at 2σ deviations. We define a plateau age if more than 75% of ^{39}Ar is released in at least three or more contiguous steps, the apparent ages of which agreed to within 2σ of the integrated age of the plateau segment. In most cases, however, only pseudoplateau ages can be obtained because the released ^{39}Ar is only 75% or less.

Two muscovite samples (nos. 414 and 664-2) were collected from mica schist (Figures 2g and 2h) of the ductile sinistral strike-slip zone located in the northern Cathaysia (Figure 1), and another muscovite sample 438-2 was taken from orthogneiss in the southeastern Cathaysia. The muscovite grains of three samples appear as scaly grains, parallel to the stretching lineation, indicative of a neoblastic origin related with ductile deformation [*Charvet et al.*, 2010]. The $^{40}Ar/^{39}Ar$ analyses show considerable variation at lower temperature (LT) stages (Table S4). The degassing during middle- to high-temperature steps (800–1150°C for sample 664-2, 800–1200°C for 438-2, and 1020–1200°C for 414) display broadly consistent apparent ages and $^{38}Ar_{Cl}/^{39}Ar_K$ ratios. The corresponding gas compositions of these stages yield three pseudoplateau ages of 231.6 ± 0.3 Ma, 307.9 ± 0.7 Ma, and 234.4 ± 0.5 Ma (Figures 9a–9c), respectively. The isotopic data from these stages yield a well-defined regression line, with the corresponding initial $(^{40}Ar/^{36}Ar)_i$ values (284 ± 32 for sample 664-2, 246 ± 90 for 438-2, and 217 ± 84 for 414) plotting in the field of the atmospheric composition, but with high uncertainties.

Similarly, three newly grown biotite samples were collected from granites (nos. 704-1 and 1106-2) and biotite schist (1106-4) in which neoblastic biotites align along the dip-slip stretching lineation. Sample 704-1 is a deformed monzonitic granite in the SW Jiangshan, sample 1106-2 is a deformed K-granite in the eastern Pingxiang, and sample 1106-4 is a mica schist in the NE Hengyang (Figure 1 and Table S4). Three stepwise age spectra show relatively flat segments at high-temperature stages (~800 to ~1400°C), and three pseudoplateau ages can be obtained at 432.7 ± 0.9 Ma (sample 704-1), 427.7 ± 0.8 Ma (sample 1106-2), and 430.6 ± 0.9 Ma (sample 1106-1) (Figures 9d–9f). The initial $(^{40}Ar/^{36}Ar)_i$ values (296 ± 17, 306 ± 4, and 299 ± 2) of these steps are consistent with that of the atmosphere, and the corresponding isochron ages 434.1 ± 2.0 Ma, 427.5 ± 1.0 Ma, and 430.3 ± 1.5 Ma are thus in a good agreement with the pseudoplateau ages.

6. Discussions

6.1. Source and Petrogenesis of the Early Paleozoic and Early Mesozoic Granitic Magma

The Early Paleozoic and Early Mesozoic granitoids in the studied areas were previously considered to be generated from Proterozoic to Early Paleozoic volcanic rocks with input of mantle material [*Wu*, 2005]. Our new data indicate that these granitic rocks are characterized by (1) abundant K-feldspar phenocrysts, enrichment of muscovite and the occurrence of tourmaline (Table 1) with high total alkali and alumina contents, indicating a peraluminous composition (Figure 3c); (2) contain inherited zircon as old as Paleoproterozoic; (3) Paleoproterozoic and Mesoproterozoic Hf model ages; and (4) geochemical characteristics indicative of a late and postorogenic setting (Figure 5b). Combined with the recently published data [*Wang et al.*, 2007a, 2010; *Zhang et al.*, 2011], we consider that both the Silurian and Triassic granites were derived from the partial melting of Paleozoic and Mesoproterozoic basement rocks.

A recent study reported circa 409 Ma gabbros from a mafic-felsic complex in the SW Jiulingshan domain (Figure 1) of the southeastern Yangtze Block. The gabbros are considered to be formed by magma mixing and mingling, in which the mafic member originated from a metasomatized lithospheric mantle during the Silurian, and are interpreted to be generated through intracontinental postorogenic collapse [*Zhong et al.*, 2013]. The generation of the mafic source magmas in the Yunkai domain of the Cathaysia Block has been correlated to late Mesoproterozoic to early Neoproterozoic asthenospheric sources metasomatised by slab-derived fluids during asthenospheric upwelling in the Paleozoic, leading to the partial melting of the continental lithospheric mantle [*Wang et al.*, 2013b]. Thus, we suggest that the granitic magmas in the study area were generated mainly by partial melting of continental basement with little or no mantle contribution.

6.2. Two Phases of Ductile Deformation and Kinematics

Regional-scale folding during Early Paleozoic time was in many places accompanied by intensive thrusting and ductile shearing, which define the major structural pattern of the South China Fold Belt. Various fold structures (overturned, asymmetric, chevron, recumbent, and sheath), thrust sheets, and mylonitized zones are widely developed in the pre-Devonian domains [*Shu et al*., 1997, 2008a; *Li et al*., 2010; *Charvet et al*., 2010; *Xu et al*., 2011; and this study]. The predominant axial traces are sub-E-W trending. Contraction of 53% (an average from 11 different localities) has been determined by analysis of chevron folds in schist and gneiss rocks (this study). Loading associated with thrusting and crustal thickening led to the development of a flexural foreland [*Li et al*., 2010, 2013; *Charvet et al*., 2010] followed by a northwestward closure of the marine basins through the Late Ordovician-Silurian period [*Rong et al*., 2003, 2010, 2012].

The stereoplots of 112 measurements on lineation and foliation in the ductile zones in the Cathaysia Block are reported in this study. Southeastern Cathaysia shows that the best development of a mylonitic foliation, which dips at 56° toward 340° with a lineation that plunges at 52° to 325° (Figure 10g). In northwestern Cathaysia, the mylonitic foliation dips 52° to 165° and the lineation plunges 44° to 170° (Figure 10h). These orientations imply dip-slip type ductile shearing. Various asymmetric fabrics (quartz or feldspar augens, mica fish structure, and sigmoidal quartz pressure shadows around clasts) in the *XZ* plane of mylonite indicate a top-to-the-southeast sense of shearing (Figures 10a and 10b) in the southeastern Cathaysia Block, and a top-to-the-northwest sense of shearing in the northwestern Cathaysia Block (Figures 10c and 10d), constituting a doubly vergent orogenic system.

In the Late Paleozoic strata, asymmetric folds and mylonitic rocks are widely developed along the sub-E-W trending Shaoxing-Pingxiang fault zone. A strike-slip-type ductile deformation displays a steep foliation and subhorizontal lineation. The mylonitic foliation dips 72° toward 190°, and the stretching lineation plunges 18° to 260° (Figure 10i). Abundant kinematic indicators (asymmetric porphyroclastic grains and asymmetric quartz augens) indicate a sinistral strike-slip sense of shear (Figures 10e and 10f). This phase of deformed structures cut the earlier dip-slip shearing fabrics in areas near the northern boundary of the Cathaysia Block.

6.3. Significances of Mica $^{40}Ar/^{39}Ar$ and Zircon U-Pb Ages

The $^{40}Ar/^{39}Ar$ data on newly grown biotites from deformed K-granites and biotite schist occurring along the Shaoxing-Pingxiang fault zone show pseudoplateau ages of 433–428 Ma (Figures 9d–9f). These ages are preserved in the middle- to high-temperature steps with approximately the same initial $(^{40}Ar/^{36}Ar)_i$ values as the atmosphere, indicating that these samples are free from excess argon. Thus, these ages can be used to constrain the cooling age of the newly grown biotite, and therefore the timing of the ductile shearing/metamorphism of the deformed granite and mica schist.

Another three samples of newly grown muscovite collected from the mylonite, deformed K-granite, and muscovite schist included two samples along the Shaoxing-Pingxiang sinistral strike-slip zone and one from the Zhenghe-Dapu fault zone. The $^{40}Ar/^{39}Ar$ data on mylonitic samples (232 ± 0.3 Ma and 234 ± 0.5 Ma) (Figures 8a and 8c) are acceptable since their initial $(^{40}Ar/^{36}Ar)_i$ values are comparable with that of the atmosphere, and the nature of occurrence of the muscovite indicates that the mylonitization terminated at ~230 Ma. In contrast, the muscovite grains from the sample 438-2 (Figure 8b) yielded abnormally low initial $(^{40}Ar/^{36}Ar)_i$ values with high uncertainties at the high-temperature steps, and the corresponding pseudoplateau age (307.9 ± 0.7 Ma) could be caused by excess Ar; thus, it is geologically meaningless.

Most of the zircons analyzed in this study display oscillatory zoning structure suggesting a magmatic origin [*Hoskin and Black*, 2000] with their concordant $^{206}Pb/^{238}U$ ages indicating granitoid emplacement around 420 Ma (Table S2 and Figures 7a–7c). This age overlaps with mica $^{40}Ar/^{39}Ar$ ages in deformed K-granites, suggesting that the granitic emplacement was coeval with regional deformation and metamorphism (Figure 9). Their negative $\varepsilon Hf(t)$ values (Figure 8) of zircons support crustal melting origin.

Three granitoid samples collected from widely separated localities (the NW boundary of Cathaysia and the Jiangnan and Nanling belts) all display similar ages around 220 Ma (Figures 8d–8f) indicating the large-scale emplacement of coeval granitoids in the Early Mesozoic as have been proposed by *Wang et al*. [2014]. In these areas, neither large-scale Late Paleozoic to Early Mesozoic oceanic fragments nor a

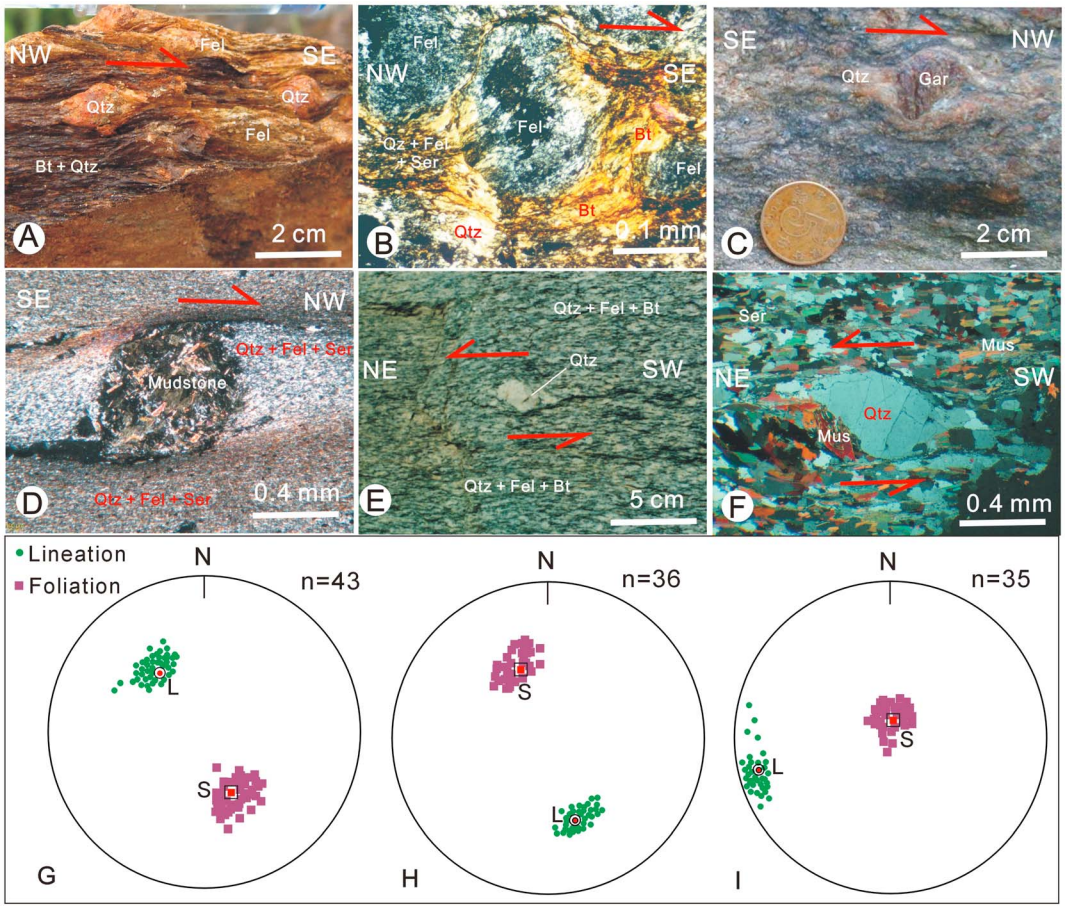

Figure 10. Outcrop photographs, photomicrographs, and stereoplots of structural data showing kinematic features in the mylonitized rocks. (a) Outcrop of the deformed K-granite (sample 112), showing a north verging movement, which was derived from asymmetric quartz augen structure, SE Cathaysia. (b) Photomicrograph of the deformed K-granite (sample 508), showing a top-to-SE sense of shear that was indicated by an asymmetric feldspar porphyroclastic system, SE Cathaysia. (c) Outcrop of the biotite schist (sample 1106-4), showing a top-to-NW movement, as inferred from the asymmetric garnet porphyroblast, NE to Hengyang (NW Cathaysia). (d) Photomicrograph of the metagreywacke, showing a top-to-NW sense of shear, which was derived from asymmetric mudstone clasts, Jinggang Mountains to the south of Pingxiang (NW Cathaysia). (e) Outcrop of the quartz-feldspar mylonite (sample 664-2), showing a sinistral strike-slip sense of shear along a NE direction, which was indicated by asymmetric quartz porphyroclast, Xinyu (the northern boundary of Cathaysia). (f) Photomicrograph of the muscovite schist (sample 414), showing a sinistral sense of shear along a NE direction, as indicated by asymmetric quartz porphyroclast, northeastern Jiangshan (the northern boundary of Cathaysia). (g–i) Stereoplots of lineation and foliation, showing the dip-slip-type deformation for Figures 10h and 10g and strike-slip-type shearing for Figure 10i, respectively (lower hemisphere, equal-area net). Qtz, quartz; Fel, feldspar; Ser, sericite; Gar, garnet; Mus, muscovite; Bt, biotite; S, pole of best computed foliation; L, axis of best computed lineation.

contemporary volcanic arc was documented, precluding active continental margin magmatism as proposed by some authors [e.g., *Xiao and He*, 2005].

6.4. Tectonic Setting of Orogenic Events

Plate margin convergent orogens (either collisional or accretionary) and intraplate orogens constitute the major types of orogenic belts [*Cawood et al.*, 2009]. Some accretionary orogenic events are followed by juvenile crust and basin development [*Kapp et al.*, 2005, 2008]. Intraplate orogens occur in regions far removed from active plate boundaries [*Cawood and Buchan*, 2007; *Cawood et al.*, 2009; *Aitken et al.*, 2013; *Raimondo et al.*, 2014] in contrast with subduction-accretion and collisional orogens. The Neoproterozoic and Phanerozoic history of central Australia [*Hand and Sandiford*, 1999; *Scrimgeour and Raith*, 2001; *Buick et al.*, 2005, 2008; *Raimondo et al.*, 2010] and the Cenozoic Tianshan belt (central Asia) [*Zhao et al.*, 2003; *Omuralieva et al.*, 2009; *Steffen et al.*, 2011] are examples of intraplate orogens.

Whether the orogenies of the Cathaysia Block during the Paleozoic were related to oceanic subduction or to an intraplate setting is unresolved. In some geodynamic reconstructions, the Cathaysia Block is located close to a plate boundary and next to the Australian continent [*Gray and Foster*, 2004; *Li et al*., 2010; *Domeier and Torsvik*, 2014]. Kyanite-bearing pelitic schists (not yet dated) and recording pressures up to 10 kbar occur in northern Cathaysia and are considered as evidence for continent-continent collision [*Zhao and Cawood*, 2012].

The Early Paleozoic and Early Mesozoic granitoids in South China are characterized by reworking of Proterozoic basement units with little or no input of a juvenile, mantle component. Geochemically, the Early Mesozoic granites are relatively more enriched in K, Si, and Al and lower in CaO content than those in the Early Paleozoic (Table S1), showing an evolutionary trend of continental crust with time, with the Early Paleozoic granitic crust evolving toward higher K, Al, and Si. Correspondingly, the Early Mesozoic granites were derived from slightly younger sources with negative εHf(t) values (average −5.4) and two-stage Hf model ages (average 1.64 Ga) in comparison with the Early Paleozoic ones with negative εHf(t) values (average −6.2) and Hf model ages (average 1.84 Ga) (Table S3 and Figure 8).

Paleozoic rocks in Cathaysia deviate from those typical of global subduction-accretion belts. These differences include: (1) lack of ophiolite, arc-type volcanic rocks and syntectonic high-pressure metamorphic rocks; (2) thick sedimentary successions that lack turbidite sequences; (3) Hf isotopic data showing that both the Silurian and the Triassic plutons were derived from partial melting of ancient crustal rocks with minor input of mantle-derived components; and (4) the >1000 km wide continuity of Early Paleozoic sedimentary sequences across Cathaysia and into the Yangtze with progressive changes in facies and no evidence for intervening continental margin assemblages [*Chen et al*., 1995, 2010, 2012; *Shu et al*., 2008a, 2014; *Wang et al*., 2010]. In addition, the Cathaysia Block in the Paleozoic was located inboard, far away from an active margin [*Zhou et al*., 2006; *Li et al*., 2010; *Zhang et al*., 2013]. Therefore, both the late Ordovician-Silurian and the Middle to Late Triassic fold-thrust zones in South China do not form part of subduction-accretion-type or subduction-collision-type orogens but likely represent an intracontinental orogen due to remote effects of plate convergence [*Li and Li*, 2007; *Li et al*., 2010; *Faure et al*., 2009; *Charvet et al*., 2010], like those in central Australia [*Raimondo et al*., 2010], the Damara Orogen of SW Africa [*Nex et al*., 2001], and the Tianshan [*Zhao et al*., 2003].

Doubly vergent thrusting can develop in convergent subduction [*Schneider et al*., 1999] or in intraplate settings [*Raimondo et al*., 2014]. Both types are associated with syntectonic magmatism, such as the western and eastern syntaxes of the Himalayas [*Treloar et al*., 2000] and the Alice Springs belt in central Australia [*Raimondo et al*., 2014]. Hence, doubly vergent thrusting does not provide a unique argument for an intraplate orogenic setting of Cathaysia in the Early Paleozoic. We presume in this study that the doubly vergent thrusting was triggered by the underthrusting or subduction of the suspected East China Sea block and of the SE Yangtze continent beneath the Cathaysia Block.

Deformation and magmatism in the Early Mesozoic in South China have been attributed as a response to the collision of the South China and North China Cratons along the Dabie-Sulu belt in the north [*Yin and Nie*, 1993; *Nie et al*., 1994; *Faure et al*., 2009], to the collision of South China and Indochina plates in the southwest [*Lepvrier et al*., 2004, 2008], or to northwestward subduction of the plaeo-Pacific plate [*Li and Li*, 2007]. Recently, regionally significant 243–220 Ma $^{40}Ar/^{39}Ar$ mica and hornblende plateau, and sensitive high-resolution ion microprobe U-Pb titanite ages were obtained from rocks in Korea [*de Jong and Ruffet*, 2014a, 2014b; *de Jong et al*., 2014]. These authors suggest that these ages are the result of a collisional event between the Japanese microplate and the East Asian continental margin in the Late Triassic [*de Jong et al*., 2009; *Kim and Ree*, 2013]. These subduction-related collision events around Cathaysia may lead to far-field intraplate tectonomagmatism in the Cathaysia Block.

6.5. Geodynamic Evolution of the South China Craton From the Middle Neoproterozoic to Early Mesozoic

Integration of data presented here with spatially and temporally available regional data from across South China enable the development of geodynamic model for its Neoproterozoic to Early Mesozoic history. Following the collision of the Yangtze and Cathaysia Blocks at 860–800 Ma [*Cawood et al*., 2013; *Yao et al*., 2014] (Figure 11a), late Neoproterozoic regional-scale extension across the assembled South China lead to

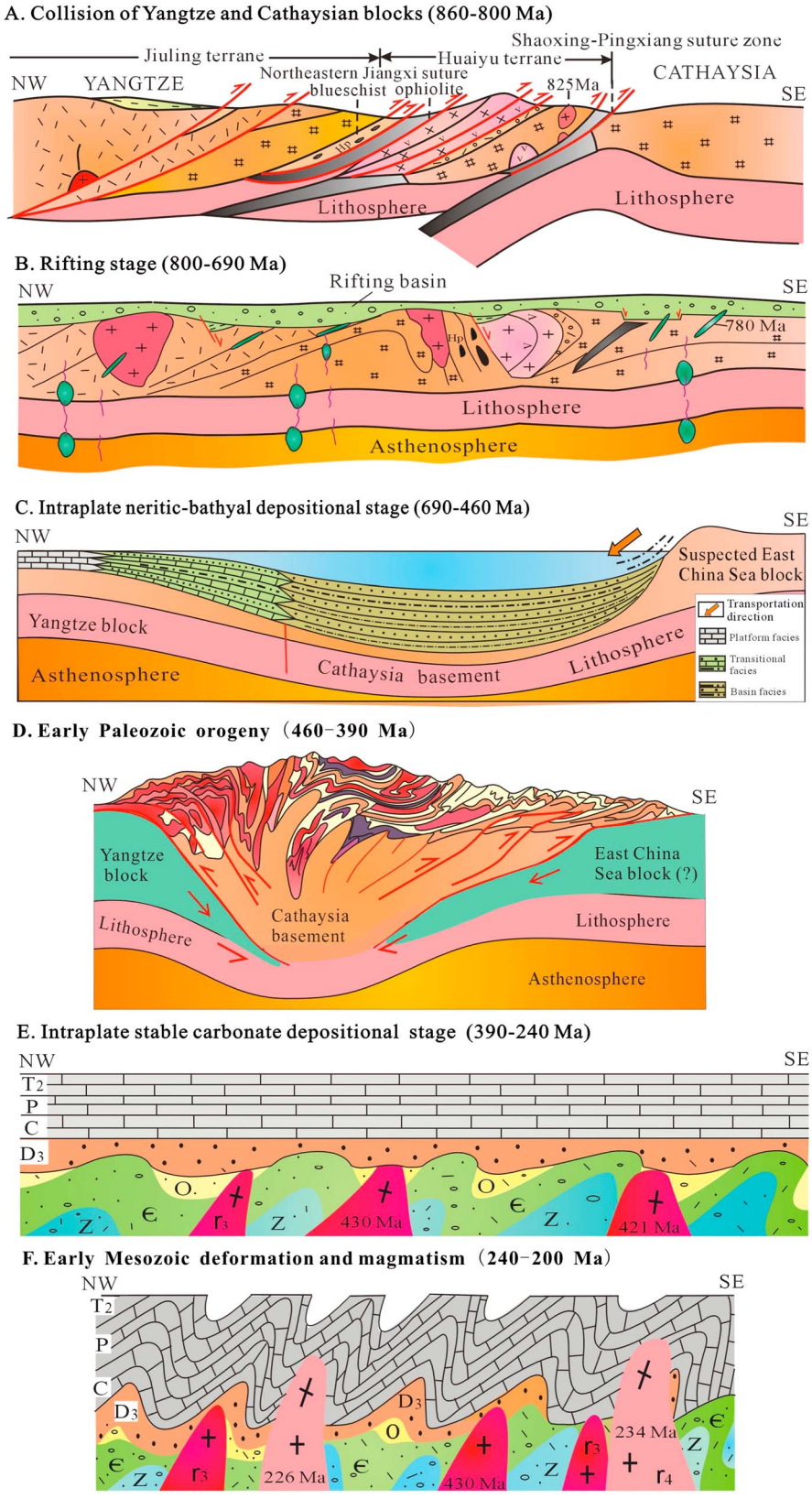

Figure 11. (a–f) Schematic illustration of the geodynamic evolution of South China, showing two-stage intracontinental deformation and magmatism in the Early Paleozoic and the Early Mesozoic after the collision of the blocks and subsequent rifting in the Neoproterozoic [modified from *Shu*, 2012]. See text for discussion.

the development of major rift basins (Figure 11b) that contain bimodal volcanic rocks dated at 800–690 Ma [*Wang and Li*, 2003]. The Cathaysia Block was split into several subblocks, including the Yunkai, Nanling, and Wuyi, and subsequently several shallow sea basins developed in the regions between these subblocks [*Shu*, 2006, 2012]. The Cathaysia Block evolved into a stable siliciclastic depositional environment (neritic-bathyal sea basin or trough) in the Sinian to Early Paleozoic (690–460 Ma) [*Shu et al*., 2014] (Figure 11c), with the absence of volcanic rocks and any evidence for input of mantle-derived components.

Since the late Ordovician, northwestward subduction of the inferred East China Sea block [*Ren*, 1964; *Ren et al*., 1990] beneath the southeastern Cathaysia Block led to strong southeast verging thrusting and amphibolite- to granulite-facies metamorphism (but not dated) in the middle to lower crust [*Zhao and Cawood*, 2012]. Meanwhile, along the Shaoxing-Pingxiang fault zone, a coeval neritic-bathyal sea block ("Pingxiang sea block") in the southeast Yangtze area was underthrust southeastward beneath the northwestern Cathaysia Block [*Zhang et al*., 2013]. This event is reflected by the northwest verging thrusts of the Cathaysia Block. The timing of this event is constrained by newly grown mica grains dated by $^{40}Ar/^{39}Ar$ analyses at 430–390 Ma [*Shu et al*., 1999; *Charvet et al*., 2010; this study]. The interaction between Cathaysia and surrounding blocks in the Early Paleozoic event resulted in the large-scale doubly vergent tectonic system. This event was followed by anatexis and emplacement of granitic magma dated at 460–390 Ma [*Shu*, 2012] (Figure 11d). The Middle to Late Devonian angular unconformity and the thick coarse-grained clastic sequence [*Shu*, 2006] provides additional evidence for Early Paleozoic orogeny.

In the Late Paleozoic (390–240 Ma), South China was characterized by a stable littoral-neritic depositional environment [*Shu et al*., 2006, 2008b, 2009] (Figure 11e) resulting in the accumulation of limestone, dolomite, and clastic rocks, with a rich flora and fauna. Since the late Middle Triassic (Ladinian) (about 240 Ma) [*Cohen et al*., 2013], the region underwent further strong deformation involving large-scale folding and thrusting of pre-Triassic strata and upwelling of peraluminous granitic magma [*Wang et al*., 2015] (Figure 11f). These deformation and magmatic events are likely a response to the collisions of the South China and North China Cratons in the North and of South China and Indochina plates in the southwest; the flat-slab subduction of the Pacific plate provides a possible trigger [*Li and Li*, 2007]. They are also considered as a response to the assembly of the Pangea supercontinent in the East Asian region [*Zhao et al*., 2006; *Zhao and Cawood*, 2012] and may be related with a possible Japanese microplate collision with the East Asian margin in the Late Triassic [*de Jong et al*., 2009].

Acknowledgments

Data supporting Figures 3–5 are available in Table S1 in the supporting information. Data supporting Figures 7–9 are available in Tables S2–S4 in the supporting information, respectively. This paper has benefited from the perceptive comments of journal reviewers P. Kapp and K. de Jong, two anonymous reviewers, and G.C. Zhao and S.Z. Li. We express our gratitude to P. Kapp and K. de Jong for their constructive suggestions and extensive annotations throughout the manuscript, which led to major improvements of the manuscript. We acknowledge financial supports provided by the National Basic Research Program of China (973 program, 2012CB416701), National Natural Science Foundation of China (41330208 and 41272226), and the Bureau of China Geological Survey (201211093-1). The paper also contributes to the 1000 Talent Award from the Chinese Government to M. Santosh.

References

Aitken, A. R. A., T. Raimondo, and F. A. Capitano (2013), The intraplate character of supercontinent tectonics, *Gondwana Res.*, *24*, 807–814.

Black, L. P., S. L. Kamo, I. S. Williams, R. Mundil, D. W. Davis, R. J. Korsch, and C. Foudoulis (2003), The application of SHRIMP to Phanerozoic geochronology: A critical appraisal of four zircon standards, *Chem. Geol.*, *200*, 171–188.

Bouvier, A., J. D. Vervoort, and P. J. Patchett (2008), The Lu–Hf and Sm–Nd isotopic composition of CHUR: Constraints from unequilibrated chondrites and implications for the bulk composition of terrestrial planets, *Earth Planet. Sci. Lett.*, *273*, 48–57.

Buick, I. S., M. Hand, I. S. Williams, J. Mawby, J. A. Miller, and B. Nicoll (2005), SHRIMP constraints on the timing of deposition of protoliths to the Harts Range Metamorphic Complex (Arunta Inlier): Tectonic implications, *J. Geol. Soc. London*, *162*, 777–787.

Buick, I. S., A. Storkey, and I. S. Williams (2008), Timing relationships between pegmatite emplacement, metamorphism and deformation during the intraplate Alice Springs Orogeny, central Australia, *J. Metamorph. Geol.*, *26*, 915–936.

Cawood, P. A., and C. Buchan (2007), Linking accretionary orogenesis with supercontinent assembly, *Earth Sci. Rev.*, *82*, 217–256.

Cawood, P. A., A. Kröner, W. J. Collins, T. M. Kusky, W. D. Mooney, and B. F. Windley (2009), Accretionary orogens through Earth history, in *Earth Accretionary Systems in Space and Time*, edited by P. A. Cawood and A. Kröner, *Geol. Soc. London Spec. Publ.*, *318*, 1–36.

Cawood, P. A., Y. J. Wang, Y. J. Xu, and G. C. Zhao (2013), Locating South China in Rodinia and Gondwana: A fragment of greater India lithosphere?, *Geology*, *41*, 903–906.

Charvet, J. (2013), The Neoproterozoic–Early Paleozoic tectonic evolution of the South China Block: An overview, *J. Asian Earth Sci.*, *74*, 198–209.

Charvet, J., L. S. Shu, M. Faure, F. Choulet, B. Wang, H. F. Lu, and N. Le Breton (2010), Structural development of the Lower Paleozoic belt of South China: Genesis of an intracontinental orogen, *J. Asian Earth Sci.*, *39*, 309–330.

Chen, X., J. Y. Rong, D. B. Rowley, J. Zhang, Y. Y. Zhang, and R. B. Zhang (1995), Is the Early Paleozoic Banxi ocean in South China necessary? [in Chinese], *Geol. Rev.*, *41*, 389–400.

Chen, X., Y. D. Zhang, J. X. Fan, J. F. Cheng, and Q. J. Li (2010), Ordovician graptolite-bearing strata in southern Jiangxi with a special reference to the Kwangsian Orogeny, *Sci. China Earth Sci.*, *53*, 1602–1610.

Chen, X., Y. D. Zhang, J. X. Fan, L. Tang, and H. Q. Sun (2012), Onset of the Kwangsian Orogeny as evidenced by biofacies and lithofacies, *Sci. China, Ser. D*, *55*, 1592–1600.

Chu, N. C., R. N. Taylor, V. Chavagnac, R. W. Nesbitt, R. M. Boella, J. A. Milton, C. R. German, G. Bayon, and K. Burton (2002), Hf isotope ratio analysis using multi–collector inductively coupled plasma mass spectrometry: An evaluation of isobaric interference corrections, *J. Anal. At. Spectrom.*, *17*, 1567–1574.

Cohen, K. M., S. C. Finney, P. L. Gibbard, and J. X. Fan (2013), The ICS International Chronostratigraphic Chart, *Episodes*, *36*, 199–204.

Cox, K. G., J. D. Bell, and R. J. Pankhurst (1979), *The Interpretation of Igneous Rocks*, 450 pp., George Allen & Unwin, London.

de Jong, K., and G. Ruffet (2014a), Tectonic implications of the very fast cooling shown by concordant 230–228 Ma $^{40}Ar/^{39}Ar$ laser probe hornblende and biotite single grain ages in the Hongseong area, *J. Geol. Soc. Korea*, *50*(5), 611–626.
de Jong, K., and G. Ruffet (2014b), 243–220 Ma $^{40}Ar/^{39}Ar$ laser probe muscovite single grain ages in the northernmost Gyeonggi Massif (Juksung area) and their tectonic implications, *J. Geol. Soc. Korea*, *50*(6), 771–782.
de Jong, K., C. Kurimoto, and G. Ruffet (2009), Triassic $^{40}Ar/^{39}Ar$ ages from the Sakaigawa unit, Kii Peninsula, Japan—Implications for possible merger of the Central Asian Orogenic Belt with large-scale tectonic systems of the East Asian margin, *Int. J. Earth Sci.*, *98*, 1529–1556.
de Jong, K., S. Han, G. Ruffet, and K. Yi (2014), First age constraints on the timing of metamorphism of the Taean Formation, Anmyeondo: Concordant 233 Ma U-Pb titanite and 231–229 Ma $^{40}Ar/^{39}Ar$ muscovite ages, *J. Geol. Soc. Korea*, *50*(5), 593–609.
Domeier, M., and T. H. Torsvik (2014), Plate tectonics in the Late Paleozoic, *Geosci. Front.*, *5*, 303–350.
Faure, M., L. S. Shu, B. Wang, J. Charvet, F. Choulet, and P. Monié (2009), Intracontinental subduction: A possible mechanism for the Early Palaeozoic Orogen of SE China, *Terra Nova*, *21*, 360–368.
Franzini, M., L. Leoni, and M. Saitta (1972), A simple method to evaluate the matrix effect in X-ray fluorescence analysis, *X-Ray Spectrom.*, *1*, 151–154.
Gray, D. R., and D. A. Foster (2004), Tectonic evolution of the Lachlan Orogen, southeast Australia: Historical review, data synthesis and modern perspectives, *Aust. J. Earth Sci.*, *51*, 773–817.
Griffin, W. L., X. Wang, S. E. Jackson, N. J. Pearson, S. Y. O'Reilly, X. S. Xu, and X. M. Zhou (2002), Zircon chemistry and magma mixing, SE China: In-situ analysis of Hf isotopes, Tonglu and Pingtan igneous complexes, *Lithos*, *61*, 237–269.
Griffin, W. L., E. A. Belousova, S. R. Shee, N. J. Pearson, and S. Y. O'Reilly (2004), Archean crustal evolution in the northern Yilgarn Craton: U-Pb and Hf-isotope evidence from detrital zircons, *Precambrian Res.*, *131*, 231–282.
Guo, L. Z., Y. S. Shi, R. S. Ma, H. G. Dong, and S. F. Yang (1989), The pre-Devonian tectonic patterns and evolution of South China, *J. Southeast Asian Earth Sci.*, *3*, 87–93.
Hand, M., and M. Sandiford (1999), Intraplate deformation in central Australia, the link between subsidence and reactivation, *Tectonophysics*, *305*, 121–144.
Harris, N. B. W., J. A. Pearce, and A. G. Tindle (1996), Geochemical characteristics of collision-zone magmatism, in *Collision Tectonics*, edited by M. P. Caward and A. C. Ries, *Geol. Soc. London Spec. Publ.*, *19*, 67–81.
Hoskin, P. W. O., and L. P. Black (2000), Metamorphic zircon formation by solid-state recrystallization of protolith igneous zircon, *J. Metamorph. Geol.*, *18*, 423–439.
Hou, K. J., Y. H. Li, T. R. Zou, X. M. Qu, Y. R. Shi, and G. Q. Xie (2007), Laser ablation–MC–ICP–MS technique for Hf isotope microanalysis of zircon and its geological applications, *Acta Petrol. Sin.*, *23*, 2595–2604.
Hsü, K. J., J. L. Li, H. H. Chen, Q. C. Wang, S. Sun, and A. M. C. Sengör (1990), Tectonics of South China: Key to understanding West-Pacific geology, *Tectonophysics*, *183*, 9–39.
Jackson, S. E., N. J. Pearson, W. L. Griffin, and E. A. Belousova (2004), The application of laser ablation-inductively coupled plasma-mass spectrometry to in situ U-Pb zircon geochronology, *Chem. Geol.*, *211*, 47–69.
Kapp, P., A. Yin, T. M. Harrison, and L. Ding (2005), Cretaceous-Tertiary shortening, basin development, and volcanism in central Tibet, *Geol. Soc. Am. Bull.*, *117*(7–8), 865–878.
Kapp, P., M. Taylor, D. Stockli, and L. Ding (2008), Development of active low-angle normal fault systems during orogenic collapse: Insight from Tibet, *Geology*, *36*(1), 7–10.
Kim, H. S., and J. H. Ree (2013), Permo-Triassic changes in bulk crustal shortening direction during deformation and metamorphism of the Taebaeksan Basin, South Korea using foliation intersection/inflection axes: Implications for tectonic movement at the eastern margin of Eurasia during the Songrim (Indosinian) orogeny, *Tectonophysics*, *587*, 133–145.
Kuiper, K. F., A. Deino, F. J. Hilgen, W. Krijgsman, P. R. Renne, and J. R. Wijbrans (2008), Synchronizing rock clocks of Earth history, *Science*, *320*, 500–504.
Lee, J. Y., K. Marti, J. P. Severinghaus, K. Kawamura, H. S. Yoo, J. B. Lee, and J. S. Kim (2006), A redetermination of the isotopic abundances of atmospheric Ar, *Geochim. Cosmochim. Acta*, *70*, 4507–4512.
Lepvrier, C., H. Maluski, and V. Nguyen (2004), The early Triassic Indosinian orogeny in Vietnam (Truong Son belt and Kontum massif); implications for the geodynamic evolution of Indochina, *Tectonophysics*, *393*, 87–118.
Lepvrier, C., V. V. Nguyen, H. Maluski, and P. Truong (2008), Indosinian tectonics in Vietnam, *C. R. Geosci.*, *340*, 94–111.
Li, H. B., D. Jia, L. Wu, Y. Zhang, H. W. Yin, G.-Q. Wei, and B.-L. Li (2013), Detrital zircon provenance of the Lower Yangtze foreland basin deposits: Constraints on the evolution of the early Palaeozoic Wuyi–Yunkai orogenic belt in South China, *Geol. Mag.*, *150*(6), 959–974.
Li, S. Z., M. Santosh, and B. M. Jahn (2012), Evolution of Asian continent and its continental margins, *J. Asian Earth Sci.*, *47*, 1–4.
Li, W. X., X. H. Li, and Z. X. Li (2005), Neoproterozoic bimodal magmatism in the Cathaysia Block of South China and its tectonic significance, *Precambrian Res.*, *136*, 51–66.
Li, W. X., X. H. Li, Z. X. Li, and F. S. Lou (2008), Obduction-type granites within the NE Jiangxi Ophiolite: Implications for the final amalgamation between the Yangtze and Cathaysia Blocks, *Gondwana Res.*, *13*, 288–301.
Li, X. H. (1997), Timing of the Cathaysia Block formation: Constraints from SHRIMP U-Pb zircon geochronology, *Episodes*, *20*, 188–192.
Li, X. H., W. X. Li, Z. X. Li, C. H. Lo, J. Wang, M. F. Ye, and Y. H. Yang (2009), Amalgamation between the Yangtze and Cathaysia Blocks in South China: Constraints from SHRIMP U–Pb zircon ages, geochemistry and Nd–Hf isotopes of the Shuangxiwu volcanic rocks, *Precambrian Res.*, *174*, 117–128.
Li, Z. X., and X. H. Li (2007), Formation of the 1300-km-wide intracontinental orogen and postorogenic magmatic province in Mesozoic South China: A flat-slab subduction model, *Geology*, *35*(2), 179–182.
Li, Z. X., et al. (2008), Assembly, configuration, and break-up history of Rodinia: A synthesis, *Precambrian Res.*, *160*, 179–210.
Li, Z. X., X. H. Li, J. A. Wartho, C. Clark, W. X. Li, C. L. Zhang, and C. M. Bao (2010), Magmatic and metamorphic events during the Early Paleozoic Wuyi-Yunkai orogeny, southeastern south China: New age constraints and P-T conditions, *Geol. Soc. Am. Bull.*, *122*, 772–793.
Lo, C. H., K. T. Howard, S. L. Chung, and S. Meffre (2002), Laser fusion $^{40}Ar/^{39}Ar$ ages of Darwin impact glass, *Meteorit. Planet. Sci.*, *37*, 1555–1562.
Ludwig, K. R. (2001), *Users Manual for Isoplot/Ex(rev.2.49): A Geochronological Toolkit for Microsoft Excel*, *Spec. Publ. 1a*, 55 pp., Geochronology Center, Berkeley, Calif.
Ma, X. X., L. S. Shu, M. Santosh, and J. Y. Li (2012), Detrital zircon U–Pb geochronology and Hf isotope data from Central Tianshan suggesting a link with the Tarim block: Implications on Proterozoic supercontinent history, *Precambrian Res.*, *206–207*, 1–16.
Maniar, P. D., and P. M. Piccolli (1989), Tectonic discrimination of granitoid, *Geol. Soc. Am. Bull.*, *101*, 635–643.
Mark, D. F., F. M. Stuart, and M. De Podesta (2011), New high-precision measurements of the isotopic composition of atmospheric argon, *Geochim. Cosmochim. Acta*, *75*, 7494–7501.

McDonough, W. F., and S. S. Sun (1995), The composition of the Earth, *Chem. Geol.*, *120*, 223–253.
Morel, M. L., A. Nebel, O. Y. J. Nebel-Jacobsen, J. S. Miller, and P. Z. Vroon (2008), Hafnium isotope characterization of the GJ-1 zircon reference material by solution and laser ablation MC–ICPMS, *Chem. Geol.*, *255*, 231–235.
Nex, P. A. M., J. A. Kinnaird, and G. J. H. Oliver (2001), Petrology, geochemistry and uranium mineralization of post-collisional magmatism around Goanikontes, southern Central Zone, Damara Orogen, Nambibia, *J. Afr. Earth Sci.*, *33*, 481–502.
Nie, S. Y., A. Yin, D. B. Rowley, and Y. G. Jin (1994), Exhumation of the Dabie-Shan ultra high pressure rocks and accumulation of the Songpan-Ganzi flysch sequence, Central China, *Geology*, *22*(11), 999–1002.
Omuralieva, A., J. Nakajima, and A. Hasegawa (2009), Three-dimensional seismic velocity structure of the crust beneath the central Tien Shan, Kyrgyzstan: Implications for large- and small-scale mountain building, *Tectonophysics*, *465*(1–4), 30–44.
Pearce, J. A. (1996), Sources and settings of granitic rocks, *Episodes*, *19*, 120–125.
Pearce, J. A., N. B. W. Harris, and A. G. Tindle (1984), Trace element discrimination diagrams for the tectonic interpretation of granitic rocks, *J. Petrol.*, *25*, 956–983.
Qi, L., and D. C. Gregoire (2000a), Determination of trace elements in twenty six Chinese geochemistry reference materials by inductively coupled plasma-mass spectrometry, *Geostand. Newsl.*, *24*, 51–63.
Qi, L., and D. C. Gregoire (2000b), Determination of trace elements in granites by inductively coupled plasma-mass spectrometry, *Talanta*, *51*, 507–513.
Raimondo, T., A. S. Collins, M. Hand, A. Walker-Hallam, R. H. Smithies, P. M. Evins, and H. M. Howard (2010), The anatomy of a deep intracontinental orogen, *Tectonics*, *29*, TC4024, doi:10.1029/2009TC002504.
Raimondo, T., M. H. William, and J. Collins (2014), Compressional intracontinental orogens: Ancient and modern perspectives, *Earth Sci. Rev.*, *130*, 128–153.
Ren, J., and T. Chen (1989), Tectonic evolution of the continental lithosphere in eastern China and adjacent areas, *J. Southeast Asian Earth Sci.*, *3*, 17–27.
Ren, J. S. (1964), A preliminary study on pre-Devonian geotectonic problems of southeastern China, *Acta Geol. Sin.*, *44*(4), 418–431.
Ren, J. S. (1991), On the geotectonics of southern China, *Acta Geol. Sin.*, *4*(2), 111–130.
Ren, J. S., T. Y. Chen, and B. G. Niu (1990), *The Tectonics and Mineralization of Continental Lithosphere in the East China and Adjacent Region* [in Chinese with English abstract], 205 pp., Science Press, Beijing.
Renne, P. R., R. Mundil, G. Balco, K. Min, and R. L. Ludwig (2010), Joint determination of ^{40}K decay constants and ^{40}Ar/^{40}K for the Fish Canyon sanidine standard, and improved accuracy for ^{40}Ar/^{39}Ar geochronology, *Geochim. Cosmochim. Acta*, *74*, 5349–5367.
Renne, P. R., G. Balco, R. L. Ludwig, R. Mundil, and K. Min (2011), Response to the comment by W.H. Schwarz et al. on "Joint determination of 40K decay constants and ^{40}Ar/^{40}K for the Fish Canyon sanidine standard, and improved accuracy for ^{40}Ar/^{39}Ar geochronology" by P.R. Renne et al. (2010), *Geochim. Cosmochim. Acta*, *75*, 5097–5100.
Rickwood, P. C. (1989), Boundary lines within petrologic diagrams which use oxides of major and minor elements, *Lithos*, *22*, 247–263.
Rong, J. Y., X. Chen, Y. Z. Su, Y. N. Ni, R. Zhanm, T. G. Chen, L. P. Fu, R. Y. Li, and J. X. Fan (2003), Silurian paleogeography of China, in *Paleography Outside of Laurentia*, edited by E. Landing and M. Johnson, *N. Y. State Museum Bull.*, *493*, 243–298.
Rong, J. Y., R. B. Zhan, H. G. Xu, B. Huang, and G. H. Yu (2010), Expansion of the Cathaysian Oldland through the Ordovician-Silurian transition: Emerging evidence and possible dynamics, *Sci. China, Ser. D*, *53*, 1–17.
Rong, J. Y., Y. Wang, and X. L. Zhang (2012), Tracking shallow marine red beds through geological time as exemplified by the lower Telychian (Silurian) in the Upper Yangtze Region, South China, *Sci. China, Ser. D*, *55*, 699–713.
Schneider, D. A., M. A. Edwards, W. S. F. Kidd, M. Asif Khan, L. Seeber, and P. K. Zeitler (1999), Tectonics of Nanga Parbat, western Himalaya: Synkinematic plutonism within the doubly vergent shear zones of a crustal-scale pop-up structure, *Geology*, *27*, 999–1002.
Scrimgeour, I., and J. G. Raith (2001), High-grade reworking of Proterozoic granulites during Ordovician intraplate transpression, eastern Arunta Inlier, central Australia, *J. Geol. Soc. London Spec. Publ.*, *184*, 261–287.
Shu, L. S. (2006), Pre-Devonian tectonic evolution of South China: From Cathaysia Block to Caledonian period folded orogenic belt [in Chinese with English abstract], *Geol. J. China Univ.*, *12*(4), 418–431.
Shu, L. S. (2012), An analysis of principal features of tectonic evolution in South China block [in Chinese with English abstract], *Geol. Bull. China*, *31*(7), 1035–1053.
Shu, L. S., H. F. Lu, J. Charvet, and M. Faure (1997), Kinematic study of the northern marginal fault zone of Wuyishan, South China [in Chinese with English abstract], *Geol. J. China Univ.*, *3*(3), 282–292.
Shu, L. S., H. F. Lu, D. Jia, J. Charvet, and M. Faure (1999), Study of the ^{40}Ar/^{39}Ar isotopic age for the Early Paleozoic tectonothermal event in the Wuyishan region, South China [in Chinese with English abstract], *J. Nanjing Univ. Nat. Sci.*, *35*(6), 668–674.
Shu, L. S., M. Faure, S. Y. Jiang, Q. Yang, and Y. J. Wang (2006), SHRIMP zircon U-Pb age, litho- and biostratigraphic analyses of the Huaiyu Domain in South China—Evidence for a Neoproterozoic orogen, not Late Paleozoic-Early Mesozoic collision, *Episodes*, *29*(4), 244–252.
Shu, L. S., J. H. Yu, D. Jia, B. Wang, W. Z. Shen, and Y. Q. Zhang (2008a), Early Paleozoic orogenic belt in the eastern segment of South China [in Chinese with English abstract], *Geol. Bull. China*, *27*(10), 1581–1593.
Shu, L. S., M. Faure, B. Wang, X. M. Zhou, and B. Song (2008b), Late Paleozoic-Early Mesozoic geological features of South China: Response to the Indosinian collision event in Southeast Asia, *C. R. Geosci.*, *340*(2–3), 151–165.
Shu, L. S., X. M. Zhou, P. Deng, B. Wang, S. Y. Jiang, J. H. Yu, and X. X. Zhao (2009), Mesozoic tectonic evolution of the southeast China block: New insights from basin analysis, *J. Asian Earth Sci.*, *34*, 376–391.
Shu, L. S., M. Faure, J. H. Yu, and B. M. Jahn (2011), Geochronological and geochemical features of the Cathaysia Block (South China): New evidence for the Neoproterozoic breakup of Rodinia, *Precambrian Res.*, *187*, 263–276.
Shu, L. S., B. M. Jahn, J. Charvet, M. Santosh, B. Wang, X. S. Xu, and S. Y. Jiang (2014), Intraplate tectono-magmatism in the Cathaysia Block (South China): Evidence from stratigraphic, structural, geochemical and geochronological investigations, *Am. J. Sci.*, *314*, 154–186.
Soderlund, U., P. J. Patchett, J. D. Vervoort, and C. E. Isachsen (2004), The ^{176}Lu decay constant determined by Lu–Hf and U–Pb isotope systematics of Precambrian basic intrusions, *Earth Planet. Sci. Lett.*, *219*, 311–324.
Steffen, R., H. Steffen, and G. Jentzsch (2011), A three-dimensional Moho depth model for the Tien Shan from EGM2008 gravity data, *Tectonics*, *30*, TC5019, doi:10.1029/2011TC002886.
Sun, S. S., and W. F. McDonough (1989), Chemical and isotopic systematics of oceanic basalts: Implications for mantle composition and processes, in *Magmatism in the Ocean Basins*, edited by A. D. Saunders and M. J. Norry, *Geol. Soc. London Spec. Publ.*, *42*, 13–345.
Treloar, P. J., D. C. Rex, P. G. Guise, J. Wheeler, A. J. Hurford, and A. Carter (2000), Geochronological constraints on the evolution of the Nanga Parbat syntaxis, Pakistan Himalaya, in *Tectonics of Nanga Parbat and the Western Himalaya*, edited by M. A. Khan et al., *Geol. Soc. London Spec. Publ.*, *170*, 137–162.

Wang, B., L. S. Shu, M. Faure, B. M. Jahn, C. H. Lo, J. Charvet, and H. S. Liu (2014), Phanerozoic multistage tectonic rejuvenation of the continental crust of Cathaysia Block: Insight from structural investigations and combined zircon U-Pb and mica $^{40}Ar/^{39}Ar$ geochronology of the granitoids of southern Jiangxi Province, *J. Geol.*, *122*(3), 309–328.

Wang, D. Z., and L. S. Shu (2012), Late Mesozoic basin and range tectonics and related magmatism in Southeast China, *Geosci. Front.*, *3*(2), 109–124.

Wang, D. Z., and X. M. Zhou (2002), *Genesis of Late Mesozoic Volcanic-Intrusive Complex of Southeast China and Crustal Evolution* [in Chinese], 202 pp., Science Press, Beijing.

Wang, H. Z., and X. X. Mo (1995), An outline of the tectonic evolution of China, *Episodes*, *18*(1–2), 6–16.

Wang, J., and Z. X. Li (2003), History of Neoproterozoic rift basins in South China: Implications for Rodinia break-up, *Precambrian Res.*, *122*(1–4), 141–158.

Wang, J. Q., L. S. Shu, M. Santosh, and Z. Q. Xu (2015), The Pre-Mesozoic crustal evolution of the Cathaysia Block, South China: Insights from zircon U–Pb geochronology, Hf isotope and REE geochemistry from the Wugongshan complex, *Gondwana Res.*, *28*, 225–245.

Wang, Y. J., W. M. Fan, G. C. Zhao, S. C. Ji, and T. P. Peng (2007a), Zircon U-Pb geochronology of gneisses in Yunkai Mountains and its implications on the Caledonian event in South China, *Gondwana Res.*, *12*(4), 404–416.

Wang, Y. J., W. M. Fan, M. Sun, X. Q. Liang, Y. H. Zhang, and T. P. Peng (2007b), Geochronological, geochemical and geothermal constraints on petrogenesis of the Indosinian peraluminous granites in the South China block: A case study in the Hunan Province, *Lithos*, *96*, 475–502.

Wang, Y. J., F. F. Zhang, W. M. Fan, G. W. Zhang, S. Y. Chen, P. A. Cawood, and A. M. Zhang (2010), Tectonic setting of the South China block in the Early Paleozoic: Resolving intracontinental and ocean closure models from detrital zircon U-Pb geochronology, *Tectonics*, *29*, TC6020, doi:10.1029/2010TC002750.

Wang, Y. J., W. M. Fan, G. W. Zhang, and Y. F. Zhang (2013a), Phanerozoic tectonics of the South China block: Key observations and controversies, *Gondwana Res.*, *23*, 1273–1305.

Wang, Y. J., A. M. Zhang, W. M. Fan, Y. H. Zhang, and Y. Z. Zhang (2013b), Origin of paleosubduction-modified mantle for Silurian gabbro in the Cathaysia Block: Geochronological and geochemical evidence, *Lithos*, *160–161*, 37–54.

Wu, F. Y., Y. H. Yang, L. W. Xie, J. H. Yang, and P. Xu (2006), Hf isotopic compositions of the standard zircons and badeleyites used in U–Pb geochronology, *Chem. Geol.*, *234*, 105–126.

Wu, H. R. (2005), Discussion on tectonopalaeogeography of Lower Yangtze area during the Caledonian Period, *J. Palaeogeogr.*, *7*(2), 243–248.

Xiang, L., and L. S. Shu (2010), Pre-Devonian tectonic evolution of the eastern south China block: Geochronological evidence from detrital zircons, *Sci. China, Ser. D*, *53*(10), 1427–1444.

Xiao, W. J., and H. Q. He (2005), Early Mesozoic thrust tectonics of the northwest Zhejiang region (Southeast China), *Geol. Soc. Am. Bull.*, *117*(7–8), 945–961.

Xu, X. B., Y. Q. Zhang, L. S. Shu, and D. Jia (2011), La-ICP-MS U-Pb and $^{40}Ar/^{39}Ar$ geochronology of the sheared metamorphic rocks in the Wuyishan: Constraints on the timing of Early Paleozoic and Early Mesozoic tectono-thermal events in SE China, *Tectonophysics*, *501*(1–4), 71–86.

Xu, Y. J., P. A. Cawood, Y. S. Du, Z. Q. Zhong, and N. C. Hughes (2014), Terminal suturing of Gondwana along the southern margin of South China Craton: Evidence from detrital zircon U-Pb ages and Hf isotopes in Cambrian and Ordovician strata, Hainan Island, *Tectonics*, *33*, 2490–2504, doi:10.1002/2014TC003748.

Yao, J. L., L. S. Shu, and M. Santosh (2011), Detrital zircon U-Pb geochronology, Hf-isotopes and geochemistry—New clues for the Precambrian crustal evolution of Cathaysia Block, South China, *Gondwana Res.*, *20*, 553–567.

Yao, J. L., L. S. Shu, M. Santosh, and G. C. Zhao (2014), Neoproterozoic arc-related mafic–ultramafic rocks and syn-collision granite from the western segment of the Jiangnan Orogen, South China: Constraints on the Neoproterozoic assembly of the Yangtze and Cathaysia Blocks, *Precambrian Res.*, *243*, 39–62.

Yin, A., and S. Y. Nie (1993), An indentation model for the North and South China collision and the development of the Tan-Lu and Honam fault systems, eastern Asia, *Tectonics*, *12*, 801–813, doi:10.1029/93TC00313.

Yu, J. H., L. J. Wang, S. Y. O'Reilly, W. L. Griffin, M. Zhang, C. Z. Li, and L. S. Shu (2009), A Paleoproterozoic orogeny recorded in a long-lived cratonic remnant (Wuyishan terrane), eastern Cathaysia Block, China, *Precambrian Res.*, *174*, 347–363.

Zhang, G. W., A. L. Guo, Y. J. Wang, S. Z. Li, Y. P. Dong, S. F. Liu, D. F. He, S. Y. Cheng, R. K. Lu, and A. P. Yao (2013), Continental tectonism and problems of South China, *Sci. China Earth Sci.*, *56*(11), 1804–1828.

Zhang, S. B., and Y. F. Zheng (2013), Formation and evolution of Precambrian continental lithosphere in south China, *Gondwana Res.*, *23*, 1241–1260.

Zhang, Y., L. S. Shu, and X. Y. Chen (2011), Study of geochemistry, geochronology and petro-genesis of the Early Paleozoic granitic plutons in the central-southern Jiangxi Province, *Sci. China Earth Sci.*, *54*, 1492–1510.

Zhao, G. C., and P. A. Cawood (1999), Tectonothermal evolution of the Mayuan assemblage in the Cathaysia Block: New evidence for Neoproterozoic collional-related assembly of the South China Craton, *Am. J. Sci.*, *299*, 309–339.

Zhao, G. C., and P. A. Cawood (2012), Precambrian geology of China, *Precambrian Res.*, *222–223*, 13–54.

Zhao, G. C., M. Sun, S. A. Wilde, S. Z. Li, and J. Zhang (2006), Some key issues in reconstructions of Proterozoic supercontinents, *J. Asian Earth Sci.*, *28*, 3–19.

Zhao, J. M., G. D. Liu, Z. X. Lu, X. K. Zhang, and G. Z. Zhao (2003), Lithospheric structure and dynamic processes of the Tianshan orogenic belt and the Junggar basin, *Tectonophysics*, *376*, 199–239.

Zhong, Y. F., C. Q. Ma, C. Zhang, S. M. Wang, Z. B. She, L. Liu, and H. J. Xu (2013), Zircon U–Pb age, Hf isotopic compositions and geochemistry of the Silurian Fengdingshan I-type granite Pluton and Taoyuan mafic–felsic complex at the southeastern margin of the Yangtze Block, *J. Asian Earth Sci.*, *74*, 11–24.

Zhou, X. M., T. Sun, W. Z. Shen, L. S. Shu, and Y. L. Niu (2006), Petrogenesis of Mesozoic granitoids and volcanic rocks in South China: A response to tectonic evolution, *Episodes*, *29*, 26–33.